AD-A077 618 SRI INTERNATIONAL MENLO PARK CA F/G 17/2.1
A SPACEDRECEIVER DATA ANALYSIS TECHNIQUE FOR SIMULTANEOUSLY EST--ETC(U)
SEP 78 C L RINO , R C LIVINGSTON DNA001-77-C-0220
UNCLASSIFIED DNA-4792T NL

1 OF 1
ADA 077618

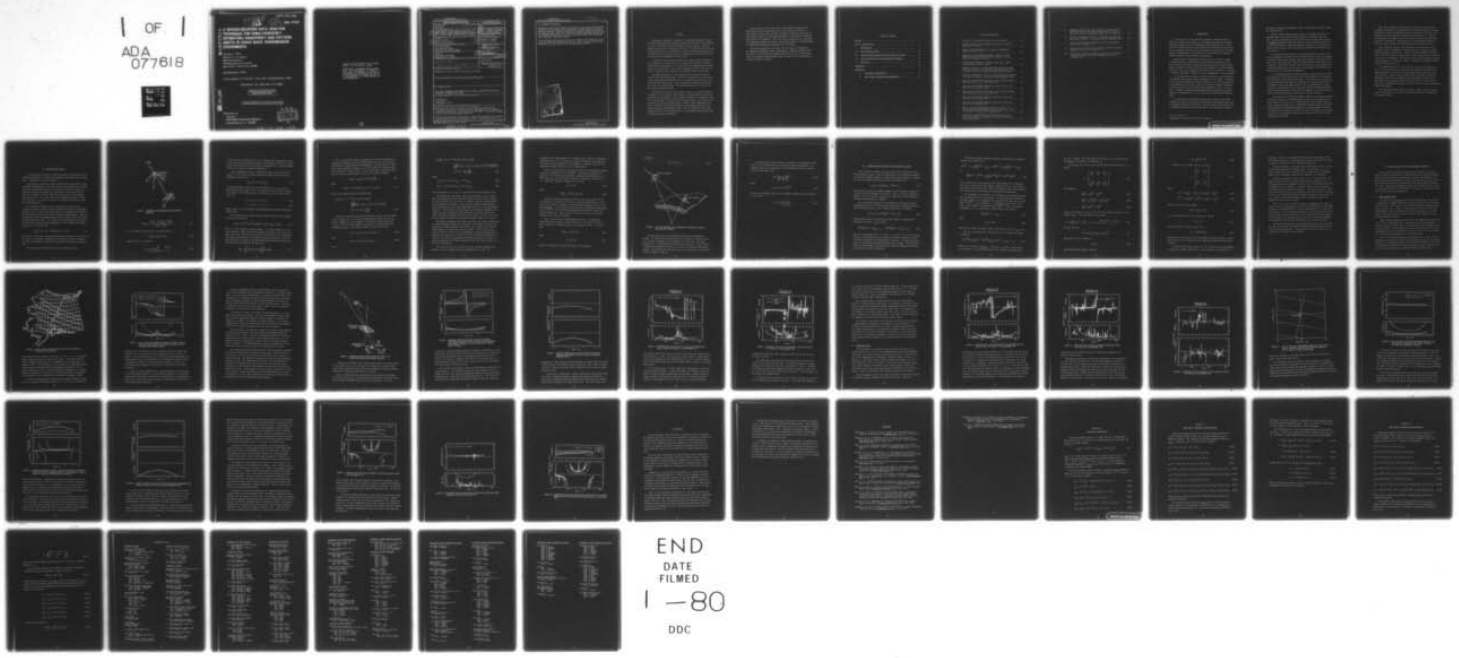

END
DATE FILMED
1 -80
DDC

A SPACED-RECEIVER DATA ANALYSIS TECHNIQUE FOR SIMULTANEOUSLY ESTIMATING ANISOTROPY AND PATTERN DRIFTS IN RADIO WAVE TRANSMISSION EXPERIMENTS

Charles L. Rino
Robert C. Livingston
SRI International
333 Ravenswood Avenue
Menlo Park, California 94025

30 September 1978

Topical Report for Period 1 June 1977—30 September 1978

CONTRACT No. DNA 001-77-C-0220

APPROVED FOR PUBLIC RELEASE;
DISTRIBUTION UNLIMITED.

THIS WORK SPONSORED BY THE DEFENSE NUCLEAR AGENCY
UNDER RDT&E RMSS CODE B322078462 I25AAXHX63340 H2590D.

Prepared for
Director
DEFENSE NUCLEAR AGENCY
Washington, D. C. 20305

Destroy this report when it is no longer needed. Do not return to sender.

PLEASE NOTIFY THE DEFENSE NUCLEAR AGENCY, ATTN: STTI, WASHINGTON, D.C. 20305, IF YOUR ADDRESS IS INCORRECT, IF YOU WISH TO BE DELETED FROM THE DISTRIBUTION LIST, OR IF THE ADDRESSEE IS NO LONGER EMPLOYED BY YOUR ORGANIZATION.

UNCLASSIFIED

SECURITY CLASSIFICATION OF THIS PAGE *(When Data Entered)*

REPORT DOCUMENTATION PAGE

READ INSTRUCTIONS BEFORE COMPLETING FORM

1. REPORT NUMBER: DNA 4792T
2. GOVT ACCESSION NO.:
3. RECIPIENT'S CATALOG NUMBER:

4. TITLE *(and Subtitle)*: A SPACED-RECEIVER DATA ANALYSIS TECHNIQUE FOR SIMULTANEOUSLY ESTIMATING ANISOTROPY AND PATTERN DRIFTS IN RADIO WAVE TRANSMISSION EXPERIMENTS

5. TYPE OF REPORT & PERIOD COVERED: Topical Report for Period 1 Jun 77—30 Sep 78

6. PERFORMING ORG. REPORT NUMBER: SRI Project 6434

7. AUTHOR(s): Charles L. Rino, Robert C. Livingston

8. CONTRACT OR GRANT NUMBER(s): DNA 001-77-C-0220

9. PERFORMING ORGANIZATION NAME AND ADDRESS: SRI International, 333 Ravenswood Avenue, Menlo Park, California 94025

10. PROGRAM ELEMENT, PROJECT, TASK AREA & WORK UNIT NUMBERS: Subtask I25AAXHX633-40

11. CONTROLLING OFFICE NAME AND ADDRESS: Director, Defense Nuclear Agency, Washington, D.C. 20305

12. REPORT DATE: 30 September 1978

13. NUMBER OF PAGES: 60

14. MONITORING AGENCY NAME & ADDRESS *(if different from Controlling Office)*: DNA, SBIE

15. SECURITY CLASS *(of this report)*: UNCLASSIFIED

15a. DECLASSIFICATION/DOWNGRADING SCHEDULE: X633

16. DISTRIBUTION STATEMENT *(of this Report)*

Approved for public release; distribution unlimited.

17. DISTRIBUTION STATEMENT *(of the abstract entered in Block 20, if different from Report)*

18. SUPPLEMENTARY NOTES

This work sponsored by the Defense Nuclear Agency under RDT&E RMSS Code B322078462 I25AAXHX63340 H2590D.

19. KEY WORDS *(Continue on reverse side if necessary and identify by block number)*

Scintillation
Striations
Irregularity Drifts

20. ABSTRACT *(Continue on reverse side if necessary and identify by block number)*

This report describes a technique for simultaneously estimating the anisotropy and relative drift of the diffraction pattern in a radio-wave transmission experiment. The technique was developed to analyze the spaced-receiver data from the Wideband Satellite.

Radio-wave scintillation data exhibit a complicated dependence on the propagation geometry relative to the magnetic field. Thus, we have also

(over)

DD FORM 1 JAN 73 1473 EDITION OF 1 NOV 65 IS OBSOLETE

UNCLASSIFIED

SECURITY CLASSIFICATION OF THIS PAGE *(When Data Entered)*

410 281

velocity

20. ABSTRACT (Continued)

developed a theory that relates the anisotropy of the measured diffraction pattern to the anisotropy of the ionospheric irregularities. The results show that one must correct the commonly used apparent velocity obtained by dividing the delay to the cross correlation function maximum into the baseline length, particularly for auroral observations where the propagation paths come near the magnetic zenith.

The preliminary results are consistent with sheet-like irregularity structures that have been hypothesized to exist in the auroral zone and highly elongated rod-like striations near the geomagnetic equator.

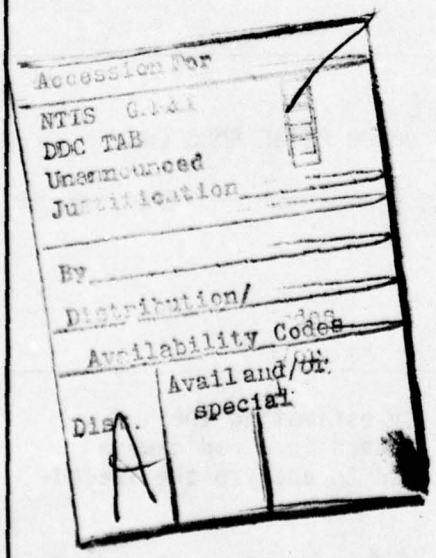

PREFACE

This report describes the analysis techniques being used to interpret the Wideband Satellite spaced-receiver data that have been routinely recorded at the Poker Flat and Kwajalein tracking stations. From the spaced-receiver data, the spatial structure of the diffraction pattern and its apparent drift can be determined. Through careful modeling, this information can be used to determine the anisotropy, effective height, and true drift of the ionospheric irregularities.

Preliminary results from the Poker Flat station confirm the sheet-like irregularity structure that we hypothesized to explain localized scintillation enhancements at the point where the propagation path intercepts the local L-shell. The auroral irregularity drifts show large impulsive variations which appear to be associated with active aurora.

The high anisotropies of the equatorial data cannot be resolved with the 900-m maximum baseline. As far as irregularity drifts are concerned, the apparent east-west drifts are largely insensitive to axial ratio increases beyond 40:1. Thus, irregularity heights and true east-west drifts can be determined. The preliminary data show evidence of the expected eastward drifts.

The analysis is done in three parts. First, the cross-correlation functions for all possible receiver pairs are measured and processed to determine the anisotropy of the diffraction pattern as a function of time for an entire pass. The measured anisotropy parameters are then used to determine the relative pattern drift. Finally, model computations are used to reproduce the measured anisotropy and apparent pattern drift, thereby giving an irregularity height. Once the height is known, the relative drifts can be converted to true irregularity drifts by removing the known satellite contribution.

Data reduction for the first part of the analysis requires much computation, which is made practical by using an array processor. A large number of passes have now been processed through the first part of the analysis, and we are developing procedures to automate the second and third parts of the analysis. This will allow accumulation of a data base of irregularity heights and drifts, which should enhance our understanding of instability mechanisms, particularly at the equator.

The model computations illustrate the importance of allowing for the geometric dependence of the scintillation. This has important ramifications for translating the Wideband satellite results to other geometries, for example, geosynchronous orbit, as well as for predicting scintillation effects in general.

TABLE OF CONTENTS

LIST OF ILLUSTRATIONS

I INTRODUCTION

In this report we first describe a general correlation function analysis technique that allows us to estimate simultaneously the anisotropy and the mean drift of a radio-wave diffraction pattern. We then develop a diffraction theory that relates the anisotropy and mean drift of the diffraction pattern to the anisotropy and mean drift of the ionospheric irregularities. The analysis has been developed to interpret Wideband Satellite spaced-receiver measurements.

Spaced-receiver measurements have been used to decades to deduce ionospheric drifts. The analysis is motivated by the principle that pairs of probes sampling a rigid but moving medium will produce similar signals displaced in time by an amount that depends on the probe separation and on the drift component along the axis of the probes. The method of similar fades (Mitra, 1949)* is a direct application of this principle.

In most applications, however, one must allow for a random diffraction pattern that undergoes some rearrangement as it drifts. Variations of the correlation method developed by Briggs et al. (1950) have proved to be superior in such cases. Indeed, the original method of Briggs et al. gives a measure of the random drift component as well as the mean drift. However, because the random component does not admit a concise physical interpretation, it is not used much now (Wright and Pitteway, 1978).

Correlation function analysis methods nearly always assume that surfaces of constant correlation are ellipsoidal and therefore give rise to elliptical contours in any plane. Various schemes have been devised to estimate the parameters that characterize the correlation ellipses.

---

*References are listed at the end of the report.

The papers by Phillips and Spencer (1955), Yerg (1955), and Fedor (1967) are representative.

However, these schemes require restrictive assumptions about the detailed shape of the spatial and/or temporal correlation functions. More recently, Armstrong and Coles (1972) devised a scheme that requires no *a priori* assumptions about the shape of the autocorrelation function or its time variation. The Armstrong-Coles method uses the intersection points of the various correlation functions obtained from different receiver pairs.

If the anisotropy is known, the intersection points provide sufficient information to determine the mean pattern drift. Thus, by assuming an isotropic diffraction pattern, Armstrong and Coles (1972) were able to measure the solar wind drift speed from interplanetary scintillation observations. They noted, however, that if the delays to the maxima of the correlation functions were also used, the anisotropy of the diffraction pattern could be determined independently.

It is interesting that the delay parameter originally used to determine the pattern drift now becomes the critical parameter for resolving the anisotropy of the diffraction pattern. This fact can be ascertained by recognizing that any change in perspective producing a high degree of correlation along a particular baseline will be interpreted as a large increase in the pattern drift if one simply divides the delay parameter into the baseline length. This effect is prominent in scintillation data from low-orbiting satellites, which are our primary interest.

In Section III we describe a general version of the Armonstrong-Coles method that allows us to simultaneously estimate the anisotopy and the mean pattern drift from a set of spaced-receiver scintillation observations. However, because of the complicated interplay between the actual three-dimensional irregularity anisotropy and the propagation geometry, in Section II we develop the diffraction theory that relates the average structure of the diffraction pattern to a general model of the average irregularity structure.

This report primarily is intended to provide a detailed and self-contained description of the spaced-receiver analysis procedures we have developed to analyze the Wideband Satellite spaced-receiver data. [The Wideband Satellite Experiment is described in Fremouw et al. (1978).] We demonstrate the method, using data from both auroral and equatorial stations, in Section IV. The results are of considerable interest in their own right, and they will be developed fully in other reports.

The preliminary results from the auroral zone data cannot be explained in terms of ionospheric irregularities that exhibit a rod-like (axially symmetric) anisotropy. We have therefore postulated a sheet-like structure in which the irregularities have a high degree of coherence transverse to the magnetic field along the direction of constant magnetic field strength, i.e., along the L-shell. Excellent results have been obtained by using this model.

The equatorial data are consistent with the expected highly elongated rod-like striations oriented along the magnetic field direction. Indeed, the axial ratio is not reliably measured with the 900-m north-south baseline. Hence, the drift rates cannot be directly measured. Nonetheless, the east-west component of the apparent pattern drift is insensitive to the precise value of the axial ratio, a, when $a \gtrsim 40$. Thus, model computations can still be used to deduce the true irregularity drifts and heights.

Both the equatorial and auroral examples clearly reveal the importance of allowing for the effects of pattern anisotropy in estimating irregularity drifts.

II THE ANISOTROPY MODEL

In this section we develop a model from which the anisotropy of the diffraction pattern in a radio-wave transmission experiment can be calculated. The geometry is shown in Figure 1.

The reference coordinate system is located within the region of the scattering irregularities. The polar angles θ and φ determine the direction of the principal ray path. If we ignore refractive effects, the principal ray path lies along the line-of-sight. The vector $\vec{B}$ is inclined at an angle ψ in the xy plane and lies along the local magnetic field vector at P. We let the z axis point downward, so that ψ is the local dip angle. A system of receivers is configured arbitrarily about the reference point R.

It is clear from Figure 1 that we must develop a fully three-dimensional model to characterize the diffracted wavefield in the neighborhood of R. To this end, we first consider the spatial autocorrelation function (ACF) of phase in the linear ray-optics approximation. That is, we calculate phase by integrating the refractive index along the direction of the principal ray path. It is shown in Rino and Fremouw (1977) that, by using this linear ray optics approximation, the spatial ACF of phase, $R_{\delta\phi}(\vec{\Delta\rho}, \Delta z; \Delta t)$, has the form:

$$R_{\delta\phi}(\vec{\Delta\rho}, \Delta z; \Delta t) = \langle \delta\phi^2 \rangle \mathcal{R}[f(\vec{\Delta\rho}_s - \vec{v}_s \Delta t)] \quad , \tag{1}$$

where $\langle \delta\phi^2 \rangle$ is the phase variance and $\mathcal{R}(y)$ gives the shape of the ACF. The fact that in a power-law environment $\langle \delta\phi \rangle^2$ depends on the data interval used (Rino and Matthews, 1978) does not affect the anisotropy considerations.

The anisotropy is characterized by the quadratic function

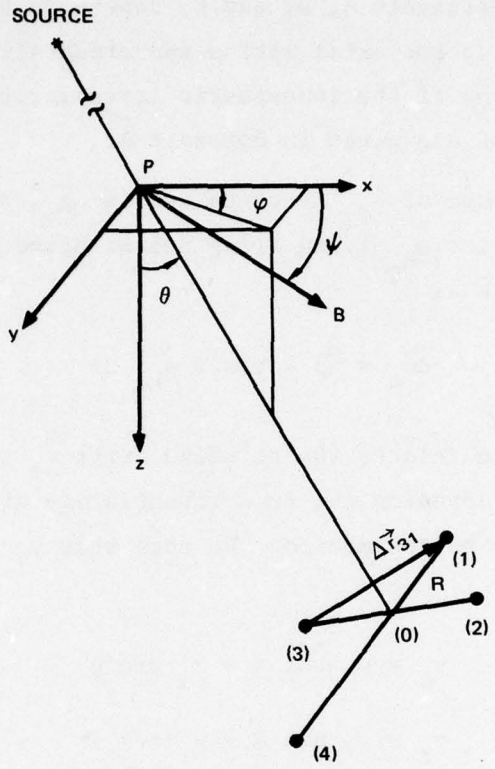

FIGURE 1 GEOMETRY FOR GENERALIZED SPACE-RECEIVER ANALYSIS

$$f^2(\Delta\vec{\rho}_s) = \frac{C\Delta\rho_{s_x}^2 - B\Delta\rho_{s_x}\Delta\rho_{s_y} + A\Delta\rho_{s_y}^2}{(AC - B^2/4)} \quad . \tag{2}$$

It is convenient to write Eq. (2) in matrix form as

$$f^2(\Delta\vec{\rho}_s) = \Delta\vec{\rho}_s^{\,T} \underset{\sim}{\mathcal{E}} \Delta\vec{\rho}_s \quad , \tag{3a}$$

where $\underset{\sim}{\mathcal{E}}$ is the 2 × 2 matrix:

$$\underset{\sim}{\mathcal{E}} = \frac{1}{AC - B^2/4} \begin{bmatrix} C & -B/2 \\ -B/2 & A \end{bmatrix} \quad . \tag{3b}$$

The anisotropy coefficients A, B, and C, depend on the propagation angles θ and φ as well as on the axial ratios and orientation angles that characterize the anisotropy of the ionospheric irregularities. Complete definitions of A, B, and C are given in Appendix A.

The Δz dependence of $R_{\delta\phi}$ is contained in $\Delta\vec{\rho}_s$, which is defined in terms of a unit vector $\hat{a}_{k_T}$ lying along the xz-plane projection of the propagation vector $\vec{k}$ as

$$\Delta\vec{\rho}_s = \vec{\Delta}\rho - \tan\theta\ \hat{a}_{k_T}\ \Delta z \quad . \tag{4}$$

A similar definition relates the relative drift $\vec{v}_s$ to v_x, v_y, and v_z. The relative drift contains the true irregularity drift and the velocity of P induced by the source motion. We note that v_y is the zonal component, and

$$v_x = v_{\parallel}\cos\psi + v_{\perp}\sin\psi \tag{5a}$$

$$v_z = v_{\parallel}\sin\psi - v_{\perp}\cos\psi \quad , \tag{5b}$$

where $v_{\parallel}$ and $v_{\perp}$ are the parallel and perpendicular meridional components, respectively.

The two-dimensional spectral density function (SDF) that corresponds to Eq. (1) has the form

$$\Phi_{\delta\phi}(\vec{\kappa}) = r_e^2\lambda^2 L\sec^2\theta\ ab\langle\Delta N_e^2\rangle\ Q\ (A\kappa_x^2 + B\kappa_x\kappa_y + C\kappa_y^2) \quad , \tag{6}$$

where r_e is the classical electron radius, λ is the wavelength, L is the layer thickness, $\langle\Delta N_e^2\rangle$ is the electron density variance, and a and b are axial ratios that characterize the degree of anisotropy of the irregularities along and transverse to the magnetic field respectively. The function Q(q) gives the shape of the three-dimensional irregularity SDF, and $\mathcal{P}(y)$ and Q(q) are related by the expression

$$\mathcal{P}(y) = \int_0^\infty qJ_o(qy)\ Q(q)dq \Big/ \int_0^\infty qQ(q)dq \quad . \tag{7}$$

Thus, to the extent that the anisotropy of the measured phase and intensity correlation functions is characterized by Eq. (2) the data interpretation is comparatively straightforward. To investigate the validity of this assumption, therefore, we first consider the intensity ACF under conditions of weak scatter. It is shown in Rino and Fremouw (1977) that the intensity SDF, $\Phi_{\delta I}(\vec{\kappa})$, is given by the simple relation

$$\Phi_{\delta I}(\vec{\kappa}) = 4\Phi_{\delta\phi}(\vec{\kappa}) \sin^2 \left[h(\vec{\kappa}) \frac{\lambda z}{4\pi}\right] \quad , \tag{8}$$

where

$$h(\vec{\kappa}) = \kappa^2 + \tan^2 \theta(\kappa_x \cos \varphi + \kappa_y \sin \varphi)^2 \quad . \tag{9}$$

Thus, the intensity ACF has the general form

$$R_{\delta I}(\Delta\vec{\rho}, \Delta z; z) = 4r_e^2 \lambda L \sec^2 \theta \, ab\langle \Delta N_e^2 \rangle \times \iint Q[A\kappa_x^2 + B\kappa_x\kappa_y + C\kappa_y^2] \sin^2 \left[h(\vec{\kappa}) \frac{\lambda z}{4\pi}\right] \times \cos \left[\vec{\kappa} \cdot \Delta\vec{\rho}_s\right] \frac{d\vec{\kappa}}{(2\pi)^2} \quad . \tag{10}$$

Because of the anisotropic diffraction term in Eq. (10), the anisotropy of $R_{\delta I}(\Delta\vec{\rho}, \Delta z; z)$ is strictly characterized by Eq. (2) only in special situations. As an example, for isotropic irregularities $A\kappa_x^2 + B\kappa_x\kappa_y + C\kappa_y^2 = h(\vec{\kappa})$ [see Appendix A], and Eq. (2) characterizes the anisotropy of $R_{\delta I}$. If we change variables in Eq. (10) so that

$$q_x = (\kappa_x \cos \varphi + \kappa_y \sin \varphi) \sec \theta \tag{11a}$$

and

$$q_y = (-\kappa_x \sin \varphi + \kappa_y \cos \varphi) \quad , \tag{11b}$$

then

$$R_{\delta I}(\Delta\vec{\rho}_s'; \Delta z, z) = 4r_e^2 \lambda^2 (L \sec\theta)\, ab\langle \Delta N_e^2 \rangle$$

$$\times \iint Q(A'q_x^2 + B'q_x q_y + C'q_y^2) \sin^2\left[q^2 \frac{\lambda(z \sec\theta)}{4\pi}\right]$$

$$\times \cos(\vec{q} \cdot \Delta\vec{\rho}_s') \frac{d\vec{q}}{(2\pi)^2} \quad , \tag{12}$$

where

$$\Delta\rho_{s_x}' = [\cos\varphi \cos\theta\, \Delta\rho_{s_x} - \sin\varphi\, \Delta\rho_{s_y}] \tag{13a}$$

$$\Delta\rho_{s_y}' = [\sin\varphi \cos\theta\, \Delta\rho_{s_x} + \cos\varphi\, \Delta\rho_{s_y}] \quad . \tag{13b}$$

The coefficients A′, B′, and C′ are defined in Rino and Fremouw (1977).

The diffraction term in Eq. (12) is now isotropic, and it follows that the anisotropy of $R_{\delta I}$ in the $\Delta\vec{\rho}_s'$ plane is given by Eq. (2) with A, B, and C replaced by A′, B′, and C′. Moreover, the same transformation can be applied to the phase, so that both the phase and amplitude have the same anisotropy in the $\Delta\vec{\rho}_s'$ plane which is normal to the propagation direction. This reference system, which was introduced by Briggs et al., (1950) and used by Singleton (1970), Moorcroft and Arima (1972), and others, generally simplifies the form of the results, but it is not completely general unless the transformation defined by Eq. (13) is used.

The analysis presented here shows that there are subtle, diffraction-induced differences between the anisotropy of the spatial structure of diffracted wavefield and that given by Eq. (2). However, for moderate zenith angles, the differences are quite small. If we consider that multiple scatter effects can be accommodated by iteratively applying the weak-scatter results (Rino, 1978), it follows that multiple-scatter effects do not change the anisotropy, although the shape of the ACFs of phase and intensity may change dramatically from that given by Eqs. (1) and (12) respectively.

One must also keep in mind that in a real (curved) ionosphere the angles θ, φ, and ψ change along the propagation path. Thus, for

propagation at oblique angles in an extended region, there is a geometric smearing effect. In our analysis, we ignore the geometric smearing and are content with obtaining a set of effective or average values for the anisotropy, height, and drift of the irregularities.

Thus, we proceed under the assumption that Eq. (2) adequately characterizes the anisotropy of the wavefield. The receiver baselines are specified in an earth-fixed geographic coordinate system (Figure 2). If $\Delta\vec{R}^T = (\Delta x_R, \Delta y_R, \Delta z_R)$ represents a particular baseline, then there is a 3 X 2 matrix $\underset{\sim}{S'}$ (defined in Appendix B) such that

$$\Delta\vec{\rho}_s = \underset{\sim}{S'}\ \vec{\Delta R} \quad . \tag{14}$$

Hence,

$$f^2(\Delta\vec{\rho}_s) = \vec{\Delta R}^T\ \underset{\sim}{S'}^T\ \underset{\sim}{\mathcal{E}}\ \underset{\sim}{S'}\ \vec{\Delta R} \quad . \tag{15}$$

Ideally one would determine the matrix $\underset{\sim}{S'}$ and then use Eq. (14) to calculate $\Delta\vec{\rho}_s$ to interpret a particular correlation measurement. As we have noted, however, $\underset{\sim}{S'}$ depends on the irregularity height, which is not known a priori. As we shall see in Section III, estimating the anisotropy and drift from a set of correlation function observations requires extensive computation. Hence, it is not practical to iterate the entire procedure for a number of heights.

Thus, we have adopted an approximate procedure by ignoring any height differences among the various receivers. We take $\underset{\sim}{S''}$ as the 2 X 2 matrix obtained by deleting the s'_{13} and s'_{23} elements in $\underset{\sim}{S'}$. It follows that

$$f^2(\Delta\vec{\rho}_s) = \vec{\Delta R}'^T\ \hat{\underset{\sim}{\mathcal{E}}}\ \vec{\Delta R}' \quad , \tag{16}$$

where

$$\hat{\underset{\sim}{\mathcal{E}}} = \underset{\sim}{S''}^T\ \underset{\sim}{\mathcal{E}}\ \underset{\sim}{S''} \tag{17}$$

and $\vec{\Delta R}'$ is obtained from $\vec{\Delta R}$ by deleting the Δz_R component.

Similarly,

$$\hat{\vec{v}}_s = [\underset{\sim}{S''}]^{-1} \vec{v}_s \quad . \tag{18}$$

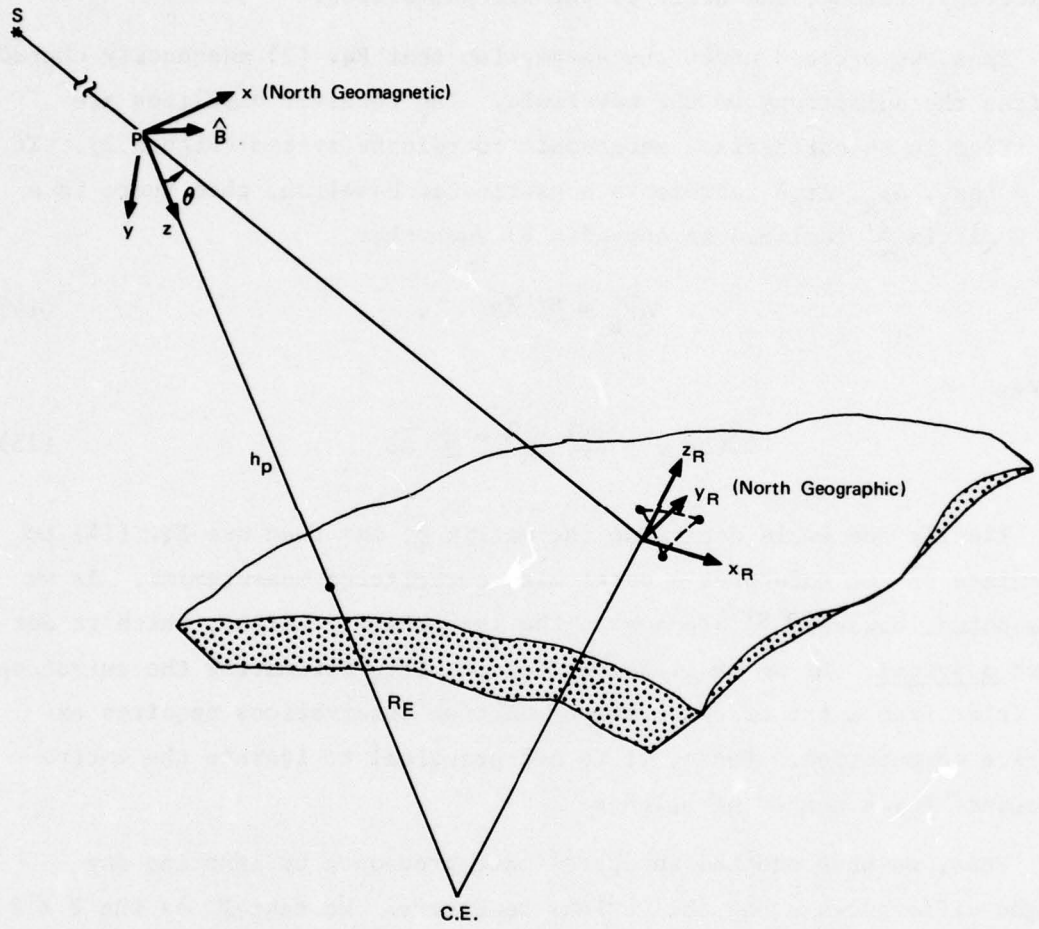

FIGURE 2 RELATION BETWEEN LOCAL GEOMAGNETIC COORDINATE SYSTEM P AND RECEIVER SYSTEM R

The anisotropy and drift parameters $\hat{\underset{\sim}{\mathcal{E}}}$ and $\hat{\vec{v}}_s$ are independent of height. The fundamental quantities $\underset{\sim}{\mathcal{E}}$ and $\vec{v}_s$ can then be computed easily for a variety of heights by inverting Eqs. (17) and (18). The final parameter set is determined by calculating the variation of $\hat{\underset{\sim}{\mathcal{E}}}$ and $\hat{\vec{v}}_s$ for a satellite pass with an assumed set of axial ratios and an irregularity height. The theoretically calculated values are compared to the measured values to obtain a best fit.

In Section III we shall describe a procedure for estimating $\hat{\underset{\sim}{\mathcal{E}}}$ and $\hat{\vec{v}}_s$ from a set of spaced-receiver correlation function measurements. For display purposes, the anisotropy of the diffraction pattern is characterized by the axial ratio,

$$\hat{AR} = \left[\frac{\hat{A} + \hat{C} + \hat{D}}{\hat{A} + \hat{C} - \hat{D}}\right]^{1/2} , \tag{19a}$$

where

$$\hat{D} = [(\hat{A} - \hat{C})^2 + \hat{B}^2]^{1/2} , \tag{19b}$$

and by the orientation angle of the principal irregularity axis relative to the y axis,

$$\hat{\delta} = \frac{1}{2} \operatorname{atan}\left[\frac{\hat{B}}{\hat{C} - \hat{A}}\right] . \tag{20}$$

III SPACED-RECEIVER ANALYSIS FOR ANISOTROPY AND DRIFT

For a system of n spaced receivers, there are n^2 temporal correlation functions, $R_{ij}(\Delta t)$, where the subscripts i and j denote the particular receivers shown in Figure 1. Based on the model described in Section II, these correlation functions will have the general form

$$R_{ij}(\Delta t) = R_{ij}[f(\vec{\Delta\rho}_{ij} - \vec{v}_s \Delta t);\ \Delta t] \quad . \tag{21}$$

In Eq. (21) we allow for temporal changes in the diffraction pattern as it drifts with the apparent velocity, $\vec{v}_s$. Thus, R_{ii} need not equal R_{jj}. However, for $i \neq j$, $R_{ij}(\Delta t) = R_{ji}(-\Delta t)$, so only $n(n + 1)/2$ correlation functions need actually be computed.

Let us now assume that the n^2 correlation functions are numbered consecutively from 1 to n^2 and denote a particular correlation function and/or baseline in this set by a single superscript, for example

$$R^{(j)}(\Delta t) = R^{(j)}[f(\vec{\Delta\rho}^{(j)} - \vec{v}_s \Delta t);\ \Delta t] \quad . \tag{22}$$

Following the method of Armstrong and Coles (1972), we identify the intercept time delay, τ_{jk}, such that

$$R^{(j)}[f(\vec{\Delta\rho}^{(j)} - \vec{v}_s \tau_{jk});\ \tau_{jk}] = R^{(k)}[f(\vec{\Delta\rho}^{(k)} - \vec{v}_s \tau_{jk});\ \tau_{jk}] \quad . \tag{23}$$

There are potentially $(n^2)^2 - n^2 - 2n(n - 1) = n(n^3 - 3n + 2)$ such intersections. The subtracted terms account for the intersections of the n^2 correlation functions with themselves and the $2n(n - 1)$ intersections between the correlation functions and their mirror images. These intersections are independent of the correlation functions themselves and therefore provide no useful information.

By using the matrix notation introduced in Section II, it follows that Eq. (23) holds only if

$$(\vec{\Delta\rho}^{(j)} - \vec{v}_s \tau_{jk})^T \underset{\sim}{\mathcal{E}} (\vec{\Delta\rho}^{(j)} - \vec{v}_s \tau_{jk}) = (\vec{\Delta\rho}^{(k)} - \vec{v}_s \tau_{jk})^T \underset{\sim}{\mathcal{E}} (\vec{\Delta\rho}^{(k)} - \vec{v}_s \tau_{jk}) \quad ,$$

or

$$\vec{v}_s^T \underset{\sim}{\mathcal{E}} (\vec{\Delta\rho}^{(j)} - \vec{\Delta\rho}^{(k)}) = \frac{1}{2\tau_{jk}} [\vec{\Delta\rho}^{(j)T} \underset{\sim}{\mathcal{E}} \vec{\Delta\rho}^{(j)} - \vec{\Delta\rho}^{(k)T} \underset{\sim}{\mathcal{E}} \vec{\Delta\rho}^{(k)}] \quad . \tag{24}$$

If $\underset{\sim}{\mathcal{E}}$ is known, Eq. (24) constitutes an overdetermined set of equations that can be solved using least squares techniques for $\vec{v}_s$. This scheme was used by Armstrong and Coles (1972) to determine solar wind velocities from spaced-receiver interplanetary scintillation measurements.

For ionospheric observations, the anisotropy of the diffraction pattern is unknown and must be determined. To determine the anisotropy, we introduce another set of equations by considering the time, lag τ_j, such that $R^{(j)}(\vec{\Delta\rho}^{(j)}; \tau_j)$ is maximized. It follows from Eqs. (21) or (22) that τ_j must minimize the quadratic form $f^2(\vec{\Delta\rho}^{(j)} - \vec{v}_s \Delta t)$. By direct computation, it can be shown that τ_j must satisfy the relation

$$\vec{v}_s^T \underset{\sim}{\mathcal{E}} \vec{\Delta\rho}^{(j)} = \tau_j v_{eff}^2 \quad , \tag{25}$$

where

$$v_{eff} = f(\vec{v}_s) \quad . \tag{26}$$

[Note that the phase ACF given by Eq. 1 has the form $\langle \delta\phi^2 \rangle \mathcal{R}(v_{eff} \Delta t)$.]

Now, if we substitute Eq. (25) into Eq. (24), we obtain the system of equations

$$\vec{\Delta\rho}^{(j)T} [\underset{\sim}{\mathcal{E}}/v_{eff}^2] \vec{\Delta\rho}^{(j)} - \vec{\Delta\rho}^{(k)T} [\underset{\sim}{\mathcal{E}}/v_{eff}^2] \vec{\Delta\rho}^{(k)} = 2\tau_{jk}(\tau_j - \tau_k) \quad , \tag{27}$$

which can be solved for $[\underset{\sim}{\mathcal{E}}/v_{eff}^2]$. Since v_{eff}^2 is simply a scale factor, the anisotropy of the diffraction patterns is completely determined by

Eq. (27). Indeed, if we divide Eq. (24) by v_{eff}^2, it is clear that knowing $[\underset{\sim}{\mathcal{E}}/v_{eff}^2]$ is sufficient to determine $\vec{v}_s$.

We can write Eq. (27) in a more compact form by defining the $N_I \times 3$ matrix

$$\mathcal{J} = \begin{bmatrix} D_{xx}^{(1)} & D_{xy}^{(1)} & D_{yy}^{(1)} \\ \cdot & \cdot & \cdot \\ \cdot & \cdot & \cdot \\ \cdot & \cdot & \cdot \\ D_{xx}^{(N_I)} & D_{xy}^{(N_I)} & D_{yy}^{(N_I)} \end{bmatrix} \tag{28}$$

with elements

$$D_{xx}^{(i)} = \Delta\rho_x^{(j)^2} - \Delta\rho_x^{(k)^2} \tag{29a}$$

$$D_{xy}^{(i)} = \Delta\rho_x^{(k)}\Delta\rho_y^{(j)} - \Delta\rho_x^{(j)}\Delta\rho_y^{(k)} \tag{29b}$$

$$D_{yy}^{(i)} = \Delta\rho_y^{(j)^2} - \Delta\rho_y^{(k)^2} \quad , \tag{29c}$$

where j and k take on all $N_I = n(n^3 - 3n + 2)$ admissible pairs of intersection values. We also define the N_I-vector,

$$\vec{T} = [2\tau_{jk}^{(1)}(\tau_j^{(1)} - \tau_k^{(1)}), \ldots\ldots\ldots, 2\tau_{jk}^{(N_I)}(\tau_j^{(N_I)} - \tau_k^{(N_I)})]^T \quad , \tag{30}$$

and the 3-vector,

$$\vec{X} = [C/v_{eff}^2, B/v_{eff}^2, A/v_{eff}^2]^T \quad . \tag{31}$$

Then Eq. (27) can be written as

$$\mathcal{J}\vec{X} = \vec{T} \quad , \tag{32}$$

which has the least squares solution

$$\hat{\vec{X}} = [\mathcal{J}^T \mathcal{J}]^{-1} \mathcal{J}^T \vec{T} \quad . \tag{33}$$

Similarly, if we define the $N_I \times 2$ matrix,

$$\mathcal{J} = \begin{bmatrix} I_x^{(1)} & I_y^{(1)} \\ \cdot & \cdot \\ \cdot & \cdot \\ \cdot & \cdot \\ I_x^{(N_I)} & I_y^{(N_I)} \end{bmatrix} \quad , \tag{34}$$

where

$$I_x^{(i)} = C(\Delta\rho_x^{(j)} - \Delta\rho_x^{(k)}) - B/2(\Delta\rho_y^{(j)} - \Delta\rho_y^{(k)}) \tag{35a}$$

$$I_y^{(i)} = -B/2(\Delta\rho_x^{(j)} - \Delta\rho_x^{(k)}) + A(\Delta\rho_y^{(j)} - \Delta\rho_y^{(k)}) \quad , \tag{35b}$$

and the N_I vector $\vec{\mathcal{J}}$ with elements

$$\vec{\mathcal{J}}^{(i)} = \tau_j^{(i)} - \tau_k^{(i)} \quad , \tag{36}$$

then, by using Eq. (27), we can rewrite Eq. (24) as

$$\mathcal{J} \vec{v}_s = \vec{\mathcal{J}} \quad . \tag{37}$$

The least-squares solution of Eq. (37) is

$$\hat{\vec{v}}_s = [\mathcal{J}^T \mathcal{J}]^{-1} \mathcal{J}^T \vec{\mathcal{J}} \quad . \tag{38}$$

Equations (33) and (38) give the anisotropy and relative pattern velocity deduced from a set of spaced-receiver temporal correlation function measurements.

To review the procedure, from a set of n spaced-receiver measurements, we generate n temporal ACFs and $n(n - 1)/2$ temporal cross-correlation

functions. This is most efficiently done by using fast Fourier transform (FFT) techniques. We then reflect the cross correlation functions to generate the basic set of n^2 correlation functions.

We next determine τ_j, the time lag at which each of the n^2 correlation functions achieves its maximum value. For the ACFs, τ_j is, of course, identically zero. Moreover, the τ_j values for sets of complementary cross correlation functions are negatives of one another.

Finally, we determine the $N_I = n(n^3 - 3n + 2)$ intersections. Here again, only half of the N_I values need actually be computed, since intersections between complementary pairs of cross correlation functions are negatives of one another. In general, however, not all possible intersections can be computed accurately. Two situations arise. First, if the correlation time is long compared to the data interval, then small errors in the correlation function estimate can lead to large errors in τ_{jk}. Second, at the other extreme of short correlation times, the intersections fall into the noise.

Thus, in our data reduction procedure we automatically reject τ_{ij} values that occur beyond some preselected decorrelation time, typically the time to 70% decorrelation. To avoid inaccuracies due to long correlation times, we reject intersections that lie outside a preselected subinterval within the data interval. One can increase the data interval to accommodate long correlation times, but this ultimately compromises the stationarity of the data, which leads to poor time resolution.

The data manipulations we have described here are rather involved, but they are practical with small, general purpose computers that have array processor capability. In Section IV, we present examples to illustrate the technique just described.

IV MODEL COMPUTATIONS AND REPRESENTATIVE EXAMPLES

In this section we apply the theory given in Section II and the method outlined in Section III to spaced-receiver data from the wideband satellite tracking stations at Poker Flat, Alaska, and Kwajalein. We first consider model computations based on the theory, use them to verify the data analysis method, and then present the representative Wideband data sets. Because the propagation geometry and irregularity structures at high latitudes differ so from those at the equator, the data from each region will be considered separately.

A. High Latitude Data

To specify the propagation angles for high latitudes, we have used a representative Wideband Satellite pass over the Poker Flat, Alaska receiving station. The satellite is in a 1000-km circular sun-synchronous orbit (Fremouw et al., 1978). The nighttime passes progress from east (premidnight) to west (postmidnight), with the trajectory of the ionospheric penetration point at a given altitude nearly parallel to the local geomagnetic meridian.

Figure 3 shows the ground projection of the 350-km penetration point for a typical postmidnight pass. The ground level constant magnetic L-shell contours are also shown to illustrate the near meridional alignment of the pass. The dip angle at the Poker Flat station is 76°. The propagation vector lies within the L shell at $L \cong 5.5$. For an overhead pass, field-aligned propagation occurs at this point.

Now, if we specify the axial ratio parameters a, b, and δ (see Appendix A), the theory developed in Section II can be used to compute the axial ratio and orientation angle of the diffraction pattern as it would be measured at the Poker Flat receiving station. Figure 4 shows the results of such computations for three different parameter sets. A

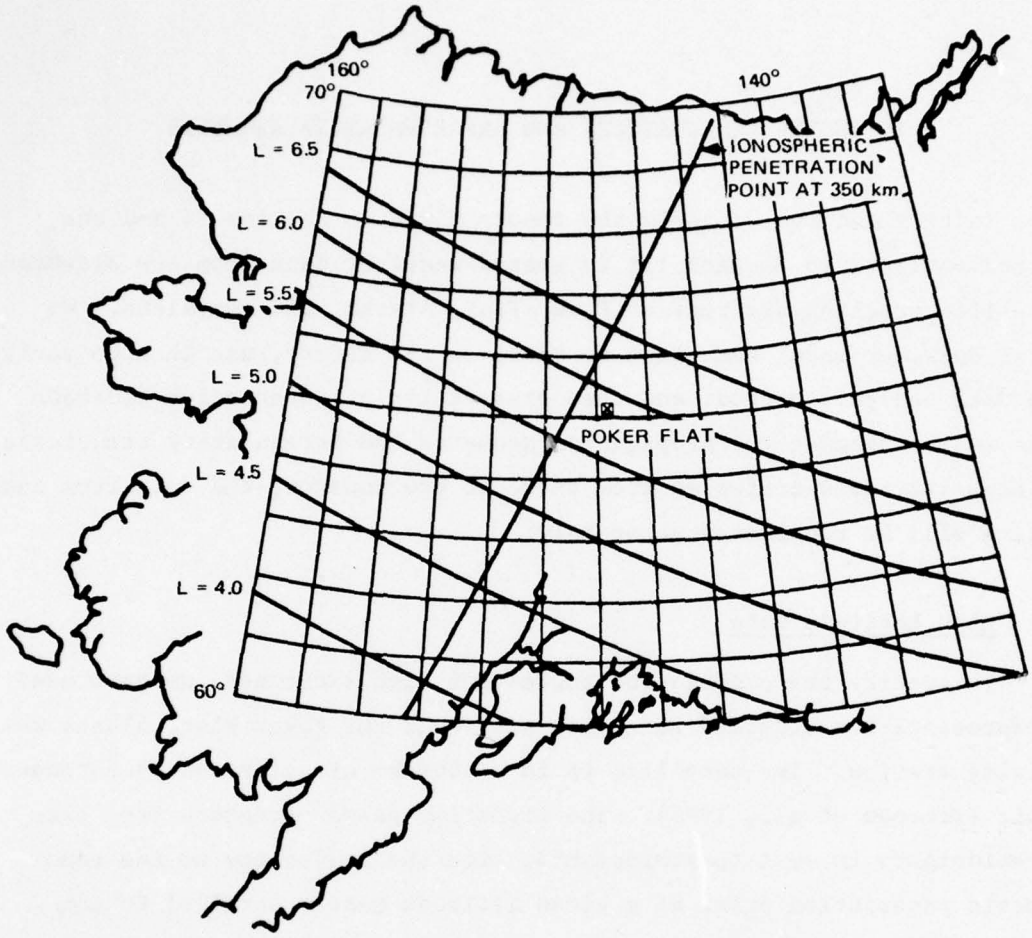

FIGURE 3 PATH OF 350-km PENETRATION FOR TYPICAL POST-MIDNIGHT WIDEBAND SATELLITE PASS

field-aligned axially symmetric structure ($a = 10$, $b = 1$, $\delta = 0$) produces highly elongated patterns at large zenith angles. The axial ratio decreases rapidly toward unity as the propagation vector approaches the magnetic zenith. The orientation of the principal axis measured relative to true north is initially along the geomagnetic meridian ($\hat{\delta} \cong 29°$). Near the magnetic zenith, the diffraction pattern undergoes a very rapid change in orientation. This effect is easily visualized if one thinks of the shadow of a rod illuminated by a moving but nonaligned source.

If the irregularities have a high degree of spatial coherence transverse to the magnetic meridian plane ($b > 1$, $\delta = 0$) as well as along the

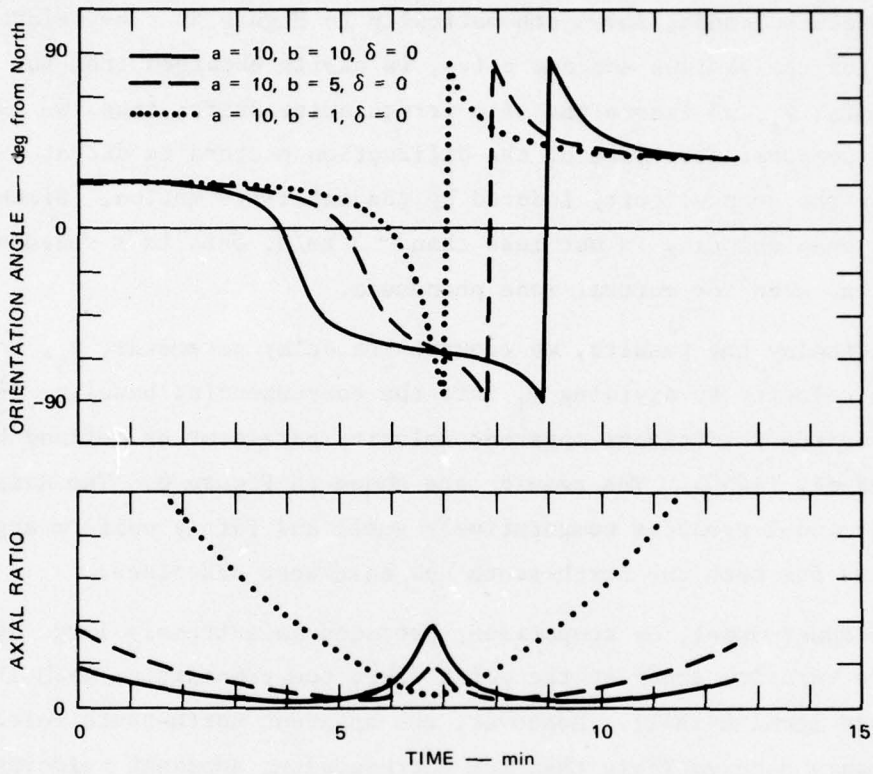

FIGURE 4 AXIAL RATIOS AND ORIENTATION ANGLES COMPUTED FOR THE HIGH-LATITUDE WIDEBAND PASS SHOWN IN FIGURE 3, USING DIFFERENT IRREGULARITY MODELS

magnetic field, the anisotropy of the diffraction pattern changes dramatically. As can be seen from the remaining two sets of curves in Figure 4, small axial ratios now occur for large zenith angles while the maximum axial ratio is achieved near the field-aligned direction where the diffraction pattern is nearly east-west aligned. Moreover, the orientation angle variations are sensitive to the degree of east-west anisotropy.

We see from these examples that, at high latitudes, the anisotropy of the diffraction pattern is a very sensitive function of the detailed irregularity anisotropy. To show this in another way, we calculated the delay time to the cross correlation peak for geomagnetic east-west and north-south aligned baselines.

The actual Wideband Satellite spaced-receiver system consists of three remote antennas, shown schematically in Figure 5. The delay parameter τ_j for the various antenna pairs, is easily obtained from Eq. (25). To determine $\vec{v}_s$, we ignore the mean irregularity drift; thus, we assume that the temporal structure of the diffraction pattern is dictated entirely by the scan velocity induced by the satellite motion. Since the F-region scan velocity is not less than $\sim$ 3 km/s, this is a reasonable assumption, even for auroral zone phenomena.

To display the results, we convert the delay parameter, τ_j, to an apparent velocity by dividing τ_j into the corresponding baseline length. This gives the traditional apparent velocity parameter as defined by Briggs et al. (1950). The results are shown in Figure 6. The axially symmetric model produces comparatively small and fairly uniform apparent velocities for both the north-south and east-west baselines.

The sheet model, by comparison, produces an extremely large apparent east-west velocity shear at the point where the propagation path lies within the local L-shell. Moreover, the apparent north-south velocity is considerably more variable than the corresponding apparent velocity for axially symmetric irregularities. These results illustrate the point made in Section I: the delay parameter τ_j can be more sensitive to the diffraction pattern anisotropy than to the relative pattern drift.

For comparison with the apparent pattern velocities shown in Figure 6, the relative pattern drift, $\vec{v}_s$, for this same pass is shown in Figure 7. In this case, of course, the relative pattern drift is due totally to satellite motion. The velocities shown are the east-west and north-south components of $\vec{v}_s$. One should keep in mind that $\vec{v}_s$ is influenced by the vertical drift component [see Eqs. (4) and (5)], and thus there will ultimately be some ambiguity in determining the meridional and zonal irregularity drifts. In the example, the drift speed is minimum at $\sim$ 3 km/s at the point of closest approach and increases monotonically for larger zenith angles. In real data, departures from this pattern indicate true irregularity drifts or irregularity height changes.

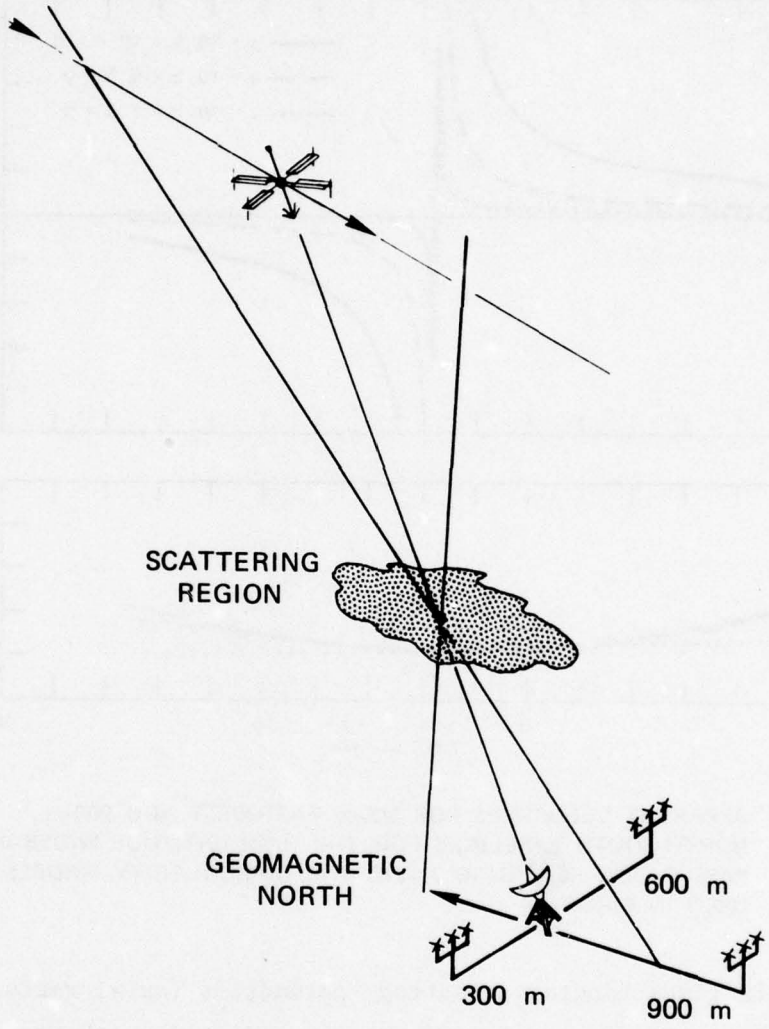

FIGURE 5 WIDEBAND SPACED-RECEIVER GEOMETRY, POKER FLAT, ALASKA AND KWAJALEIN, MARSHALL ISLANDS

Comparison of Figures 6 and 7 shows clearly that, for moving beacons in the auroral zone, it is impossible to estimate true pattern drifts, particularly east-west drifts, from measured apparent velocities without taking the irregularity anisotropy into account.

We next demonstrate the effectiveness of the intersection method, described in Section III, in extracting the anisotropy and relative drift from the actual Wideband system under ideal conditions. For these

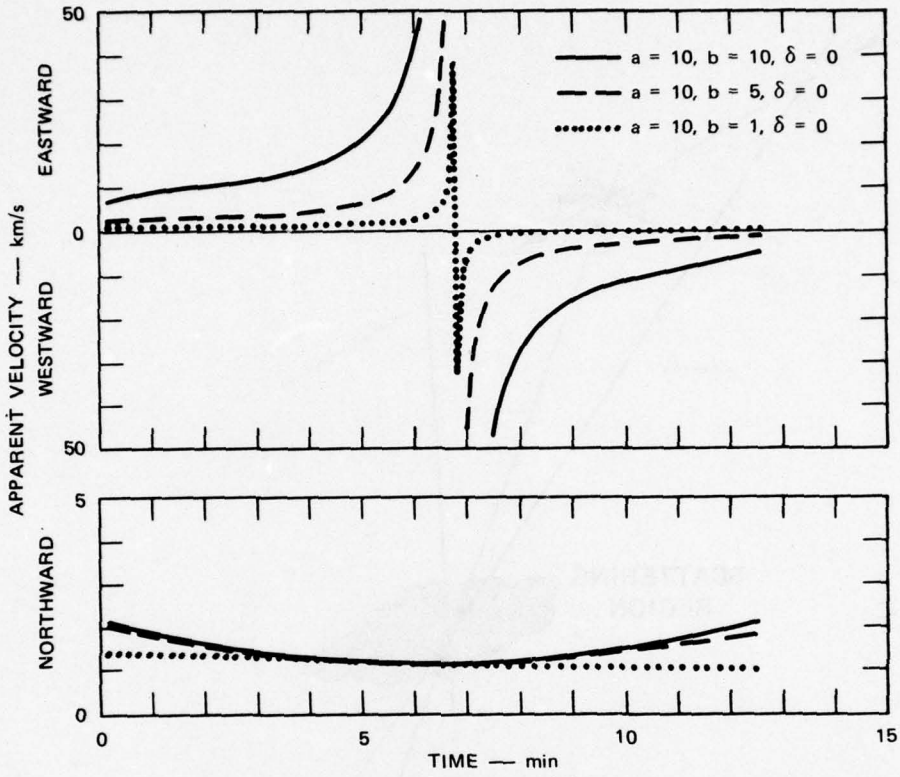

FIGURE 6 APPARENT VELOCITIES FOR 300-m EAST-WEST AND 900-m NORTH-SOUTH BASELINES FOR THE HIGH-LATITUDE WIDEBAND PASS SHOWN IN FIGURE 3 AND THE IRREGULARITY MODELS USED IN FIGURE 4

simulations, the time-changing anisotropy parameters (axial ratio, orientation, and relative pattern velocities) are predicted by the model--for each antenna and between each of the antenna pairs--and then used in place of the measured correlation functions in the analysis routine. A simple gaussian form for $R^{(j)}(y)$ [Eq. (22)] was used, with a decorrelation time similar to measured values.

The satellite pass geometry used in the simulations is that used to produce Figure 4. For the three anisotropy cases (sampled every 20 s during the pass), the largest discrepancies between the input and output parameters are: axial ratio 2% and orientation 0.01°. The errors in extracting the relative pattern drifts as shown in Figure 7, which are

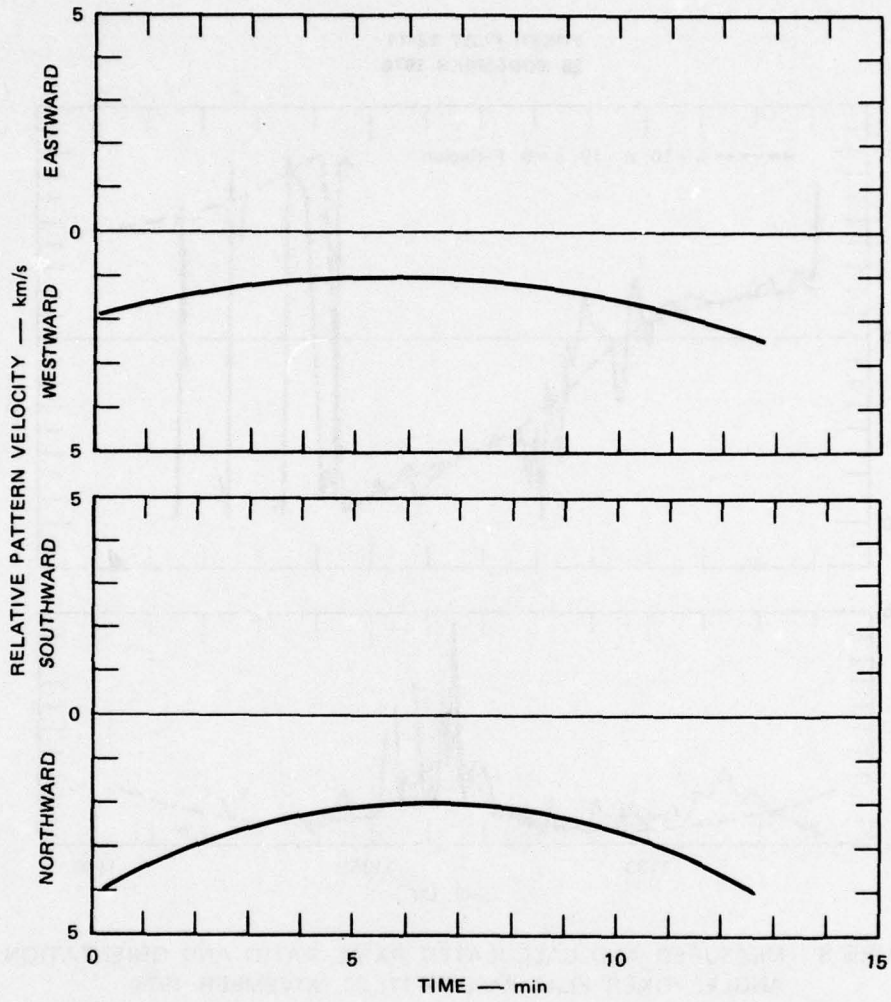

FIGURE 7 RELATIVE IRREGULARITY DRIFTS FOR THE HIGH-LATITUDE WIDEBAND PASS SHOWN IN FIGURE 3, SATELLITE-INDUCED COMPONENT ONLY

independent of the irregularity model assumed, are better than 1%, except in the region of most rapidly changing anisotropy, where errors of about 10% occur. Overall then, under ideal conditions, the extraction method works very well.

We turn now to actual data. Figure 8 shows axial ratio and orientation angle estimates obtained by applying the analysis described in Section III to Wideband Satellite UHF (413 MHz) spaced-receiver measurements made at Poker Flat for pass number 12-11. The data clearly show

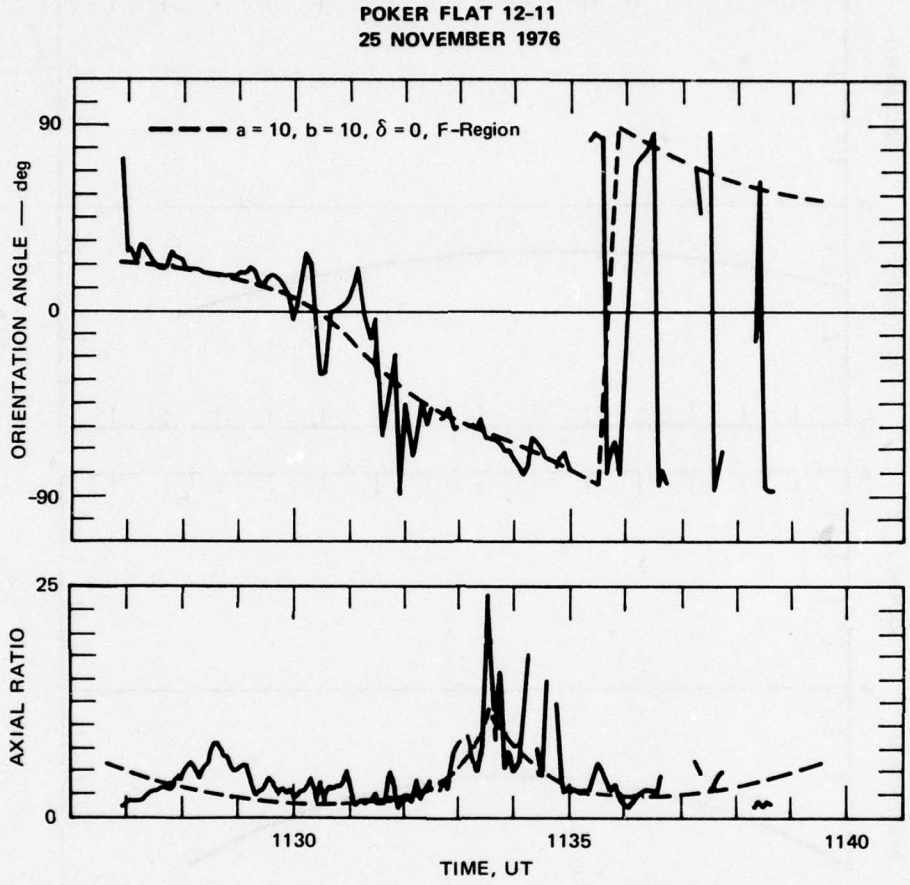

FIGURE 8 MEASURED AND CALCULATED AXIAL RATIO AND ORIENTATION ANGLE, POKER FLAT PASS 12-11, 25 NOVEMBER 1976

the enhanced axial ratios near the center of the pass that indicate sheet-like structures. Indeed, the sheet-model theory, which is superimposed on the data in Figure 8, fits exceptionally well up to ~ 1136 UT. Beyond 1136 UT, the UHF perturbations are very weak, which accounts for the large data scatter.

As one should expect, the model anisotropy computations are not particularly height-sensitive. On the other hand, the magnitude of the apparent velocities changes significantly with height. Figure 9 shows the measured apparent velocities for the same data. As was the case with Figure 6, large apparent velocities here are due to rapidly changing

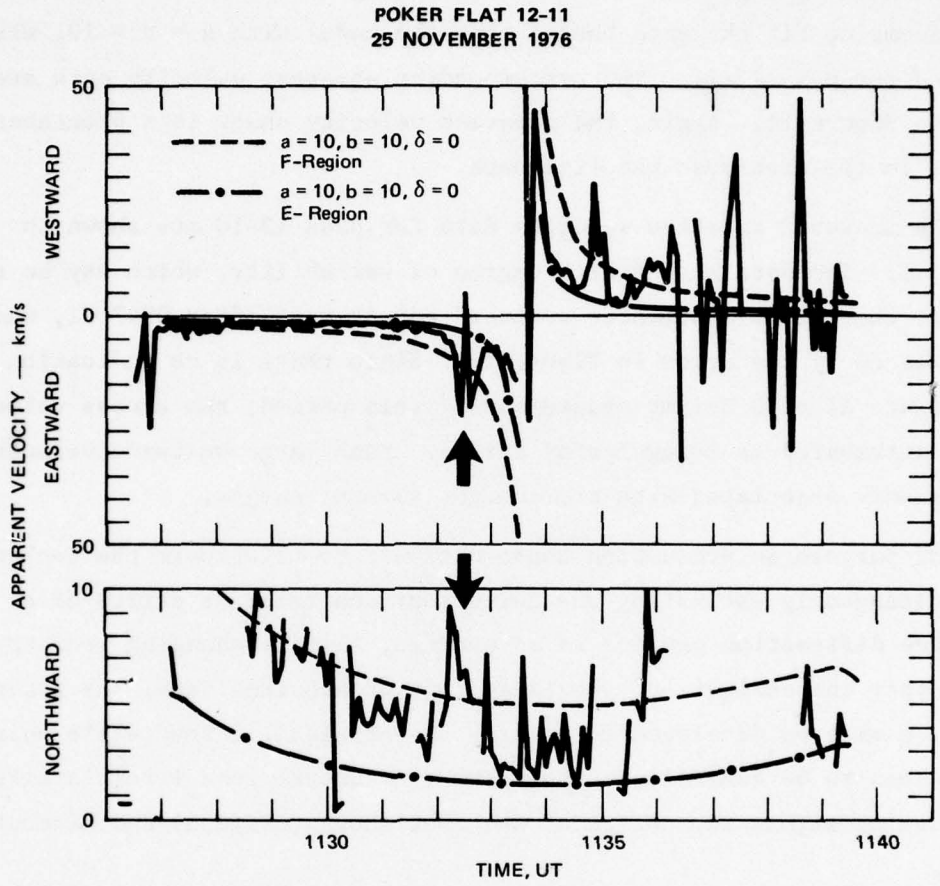

FIGURE 9 MEASURED AND CALCULATED APPARENT VELOCITIES, POKER FLAT PASS 12-11, 25 NOVEMBER 1976

irregularity anisotropy, with a prominent shear in the data from the east-west baseline.

The sheet-model data are shown for both E-region (110 km) and F-region (350 km) reference altitudes. The measured apparent velocities generally fall between the two model calculations. There is, however, a localized excursion that suggests an altitude change just after 1132 UT. This event is marked by the arrows in Figure 9. After 1133 UT, the data follow the E-region curve.

To illustrate the computation of the relative velocity, $\vec{v}_s$, we used a more uniformly disturbed pass than 12-11. The anisotropy parameters

for this data set, pass 12-10 are shown in Figure 10. A sheet model with $b < a$ seems to fit the data better than the model with $a = b = 10$, which was used for pass 12-11. The corresponding apparent velocity data are shown in Figure 11. Again, the apparent velocity shear is a prominent feature in the east-west baseline data.

The measured relative velocity data for pass 12-10 are shown in Figure 12. The data show a high degree of variability, which may be real. However, there is a systematic westward enhancement after 0947 UT, which is indicated by the arrow in Figure 12. Since there is no indication from Figure 11 of a height change during this period, the excess velocity can be attributed to irregularity drifts. Such large westward velocities are commonly associated with premidnight auroral surges.

Our purpose in presenting these data was to illustrate the technique of simultaneously estimating the anisotropy and relative drifts of a radiowave diffraction pattern in an extreme, rapidly changing geometry. As we apply the analysis to the large body of acquired data, the interpretation will be developed in detail. Nonetheless, a sheet-like anisotropy seems to be generally appropriate for auroral zone irregularities that develop within the region of the continuous (diffuse) and discrete aurora.

B. Equatorial Data

The situation at the equator is very different from that in the auroral zone, both in terms of the propagation geometry and irregularity structure. The F-region (350 km) penetration point for a near-overhead pass at the Wideband site on Kwajalein, Marshall Islands is shown in Figure 13. Such a pass scans a range of shallow dip angles, from $\sim 23°$ in the north to $\sim -8°$ in the south. As in Alaska, the F-region penetration scan is within a few degrees of the local magnetic meridian. On the ground, the spaced-receiver arrangement at Kwajalein is as shown in Figure 5, with the north-south 900-m baseline magnetically aligned.

Near the magnetic equator, the high conductivity along near-horizontal field lines creates elongated irregularity structures. Both this

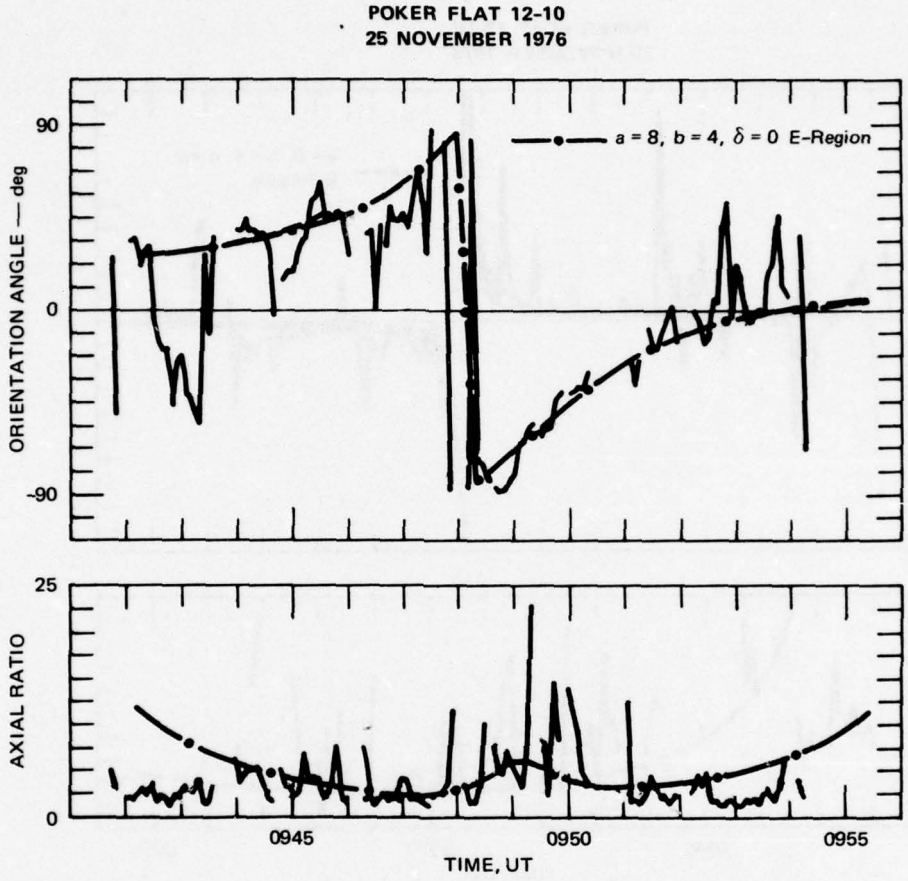

FIGURE 10 MEASURED AND CALCULATED AXIAL RATIO AND ORIENTATION ANGLE, POKER FLAT PASS 12-10, 25 NOVEMBER 1976

elongation and the near-field alignment of the satellite scan act to produce a highly elongated diffraction pattern on the ground for the entire satellite pass. To show this quantitatively, we used the theory given in Section II to compute the diffraction pattern parameters for a near overhead pass at Kwajalein. The ground pattern axial ratio and orientation for axially symmetric 10:1 rods ($a = 10$, $b = 1$, $\delta = 0$) and 50:1 rods at a 400-km altitude are shown in Figure 14. Projection of the ionospheric structure produces axial ratios a few times those of the in-situ irregularities at low elevation angles, and essentially reproduces the in-situ anisitropy near the closest approach. The orientation of the ground

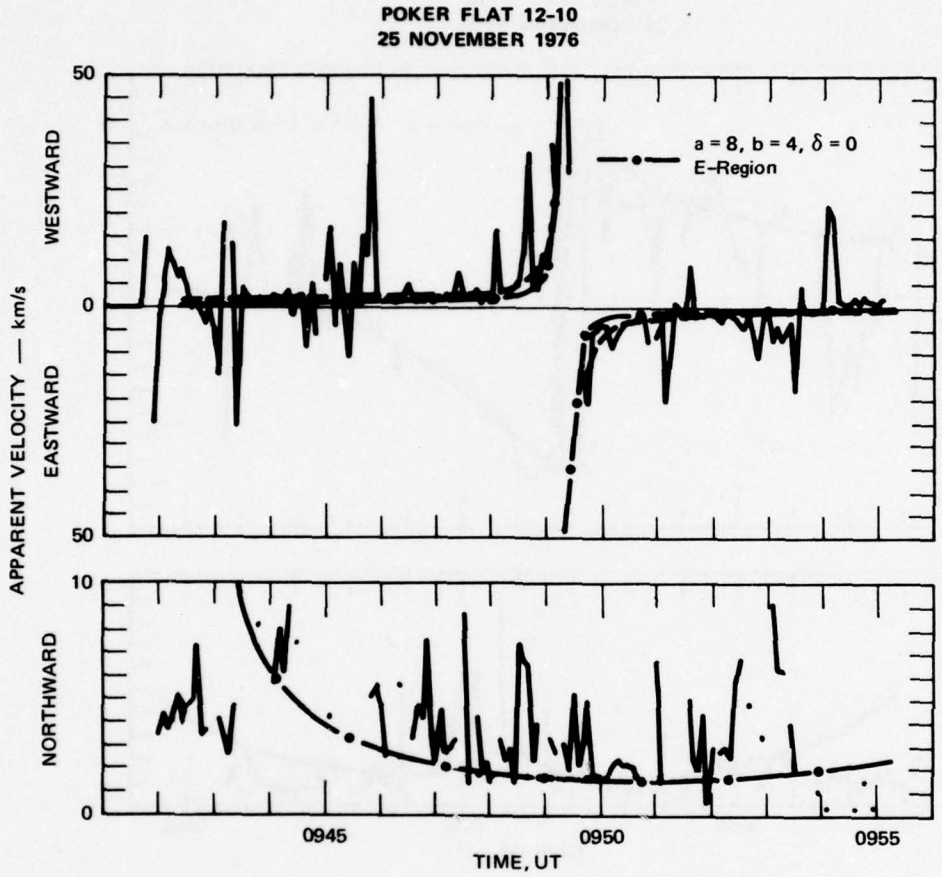

FIGURE 11 MEASURED AND CALCULATED APPARENT VELOCITIES, POKER FLAT PASS 12-10, 25 NOVEMBER 1976

correlation ellipse remains near 10 to 12 deg from geographic north during the entire pass.

The apparent velocities for this same pass geometry and irregularity structure are shown in Figure 15. The east-west apparent velocity for the rod model is a few hundred meters per second and decreases with increasing axial ratio. Beyond an axial ratio of about 50:1, the east-west apparent velocity essentially saturates and no longer decreases with increasing axial ratio. Because the propagation path is not quite in the local magnetic meridian, the satellite scan produces large, north-south, apparent velocity shears. The increase from 10:1 to 50:1 rods dramatically

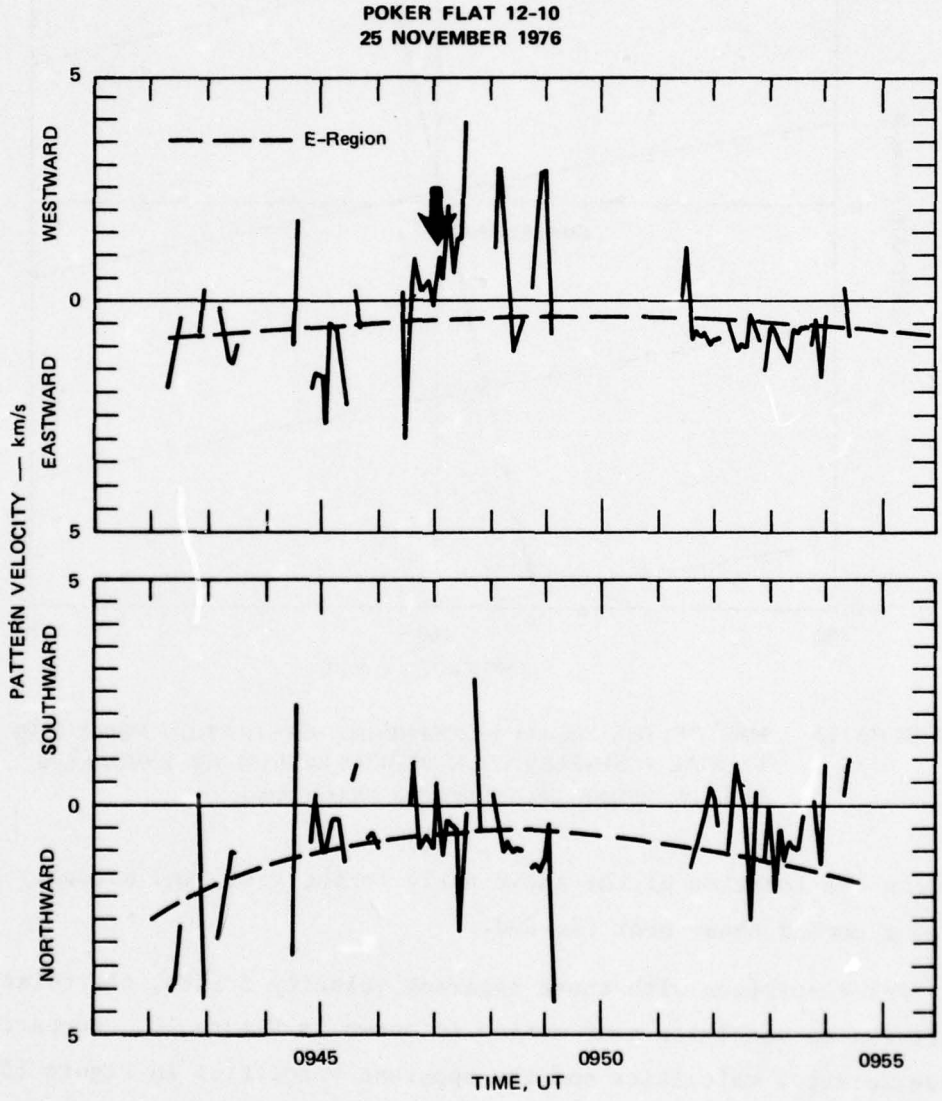

FIGURE 12 MEASURED AND CALCULATED RELATIVE VELOCITIES, POKER FLAT PASS 12-10, 25 NOVEMBER 1976

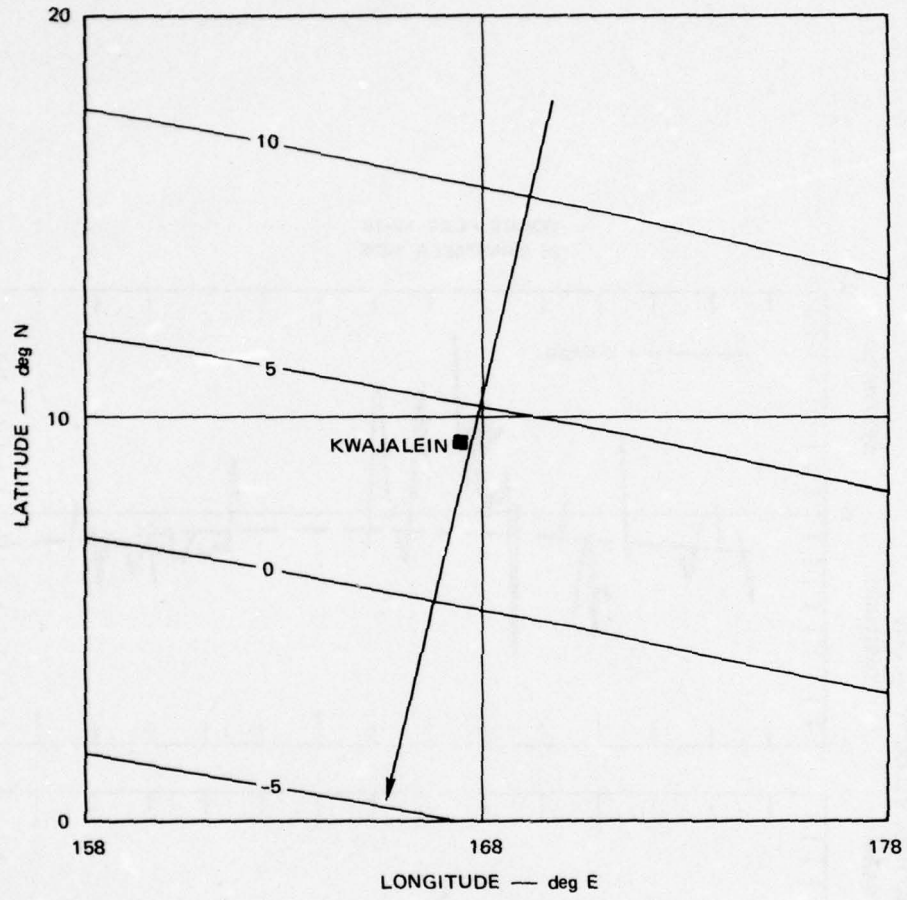

FIGURE 13 MAP OF THE 350-km IONOSPHERIC PENETRATION POINT FOR A TYPICAL HIGH-ELEVATION WIDEBAND PASS AT KWAJALEIN.
Lines of constant dip latitude are superimposed

affects the location of the shear early in the pass, and actually produces a second shear near the end.

For comparison with these apparent velocity drifts, the relative drift due to satellite scan motion is shown in Figure 16. Comparison of these relative velocities and the apparent velocities in Figure 15 show again (as at high latitudes) that for time-changing propagation geometry, removal of the anisotropy from the ground diffraction pattern is essential in interpreting apparent pattern velocities.

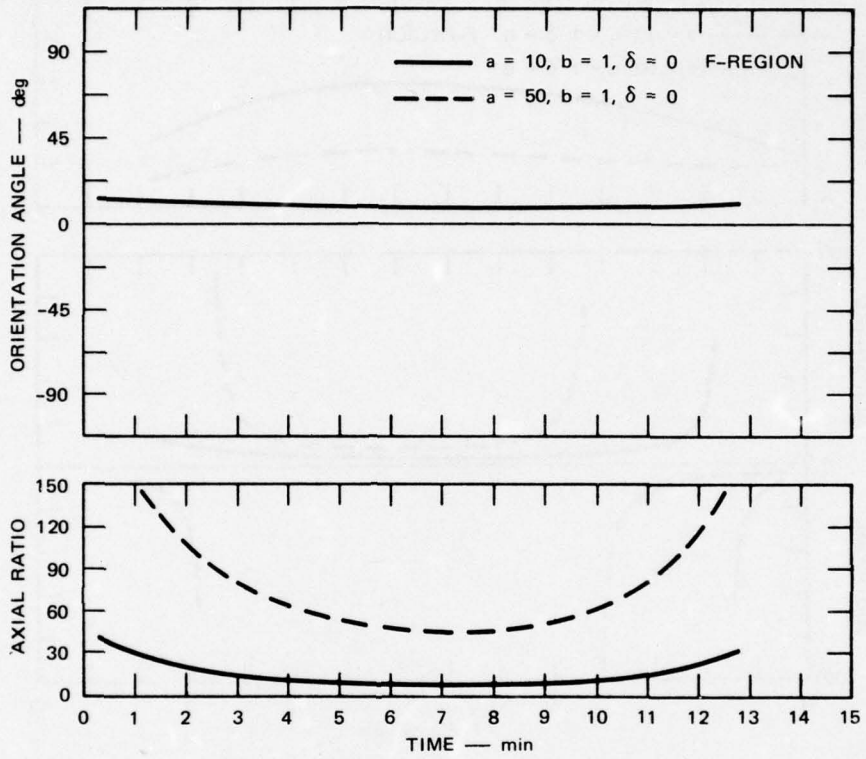

FIGURE 14 AXIAL RATIOS AND ORIENTATION ANGLES COMPUTED FOR THE EQUATORIAL WIDEBAND PASS SHOWN IN FIGURE 13 AND ROD-LIKE IRREGULARITY MODELS

One point of concern in using the intersection method on the equatorial data is whether the north-south baseline spacing of $\sim$ 900 m is adequate to measure the extreme pattern anisotropy that may occur. To ensure that the method can, in fact, resolve large axial ratios, a series of simulations, similar to those discussed earlier, have been carried out. Gaussian correlation functions with decorrelation times comparable to those in the data were again used to fully simulate the time-changing ground diffraction pattern.

Even with our relatively short baseline, the intersection method succeeds in extracting the correct axial ratio for the rod model and ground-pattern axial ratios up to about 200:1 with small errors. For example, 100:1 in-situ rods produce pattern axial ratios up to about

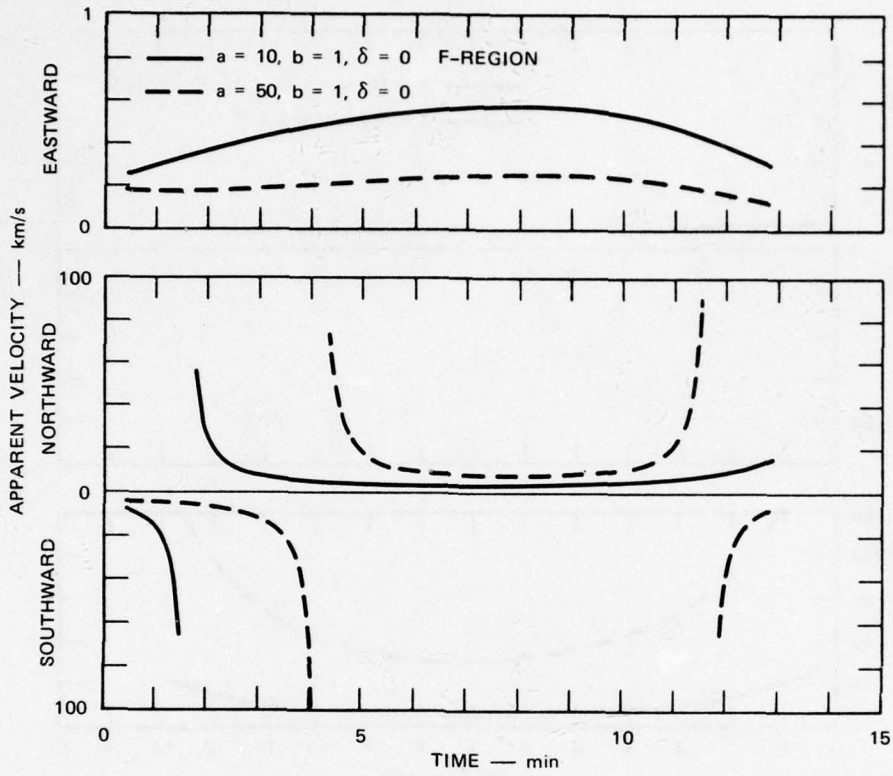

FIGURE 15 APPARENT VELOCITIES FOR 300-m EAST-WEST AND 900-m NORTH-SOUTH BASELINES FOR THE WIDEBAND EQUATORIAL PASS SHOWN IN FIGURE 13, AND THE IRREGULARITY MODELS USED IN FIGURE 14

400:1 at the horizons. Pattern axial ratios up to about 200:1 are extracted with errors less than 1%; between 200:1 and 400:1, random errors of up to 12% are observed. It is important to note, however, that although errors are seen for these high axial ratios, the method never fails to obtain an estimate [i.e., $AC > B^2/4$ for all cases, see Eq. (3)]. In no case is the orientation error greater than 0.01°.

The analysis method does not do as well in extracting the relative drift velocities. For pattern axial ratios up to about 100:1, the errors in the extracted east-west and north-south relative velocities are below $\sim$ 3%. For axial ratios between 100:1 and 150:1, random errors of up to about 20% are seen; beyond about 150:1, the intersection method generally fails to give reasonable results for relative drift velocities.

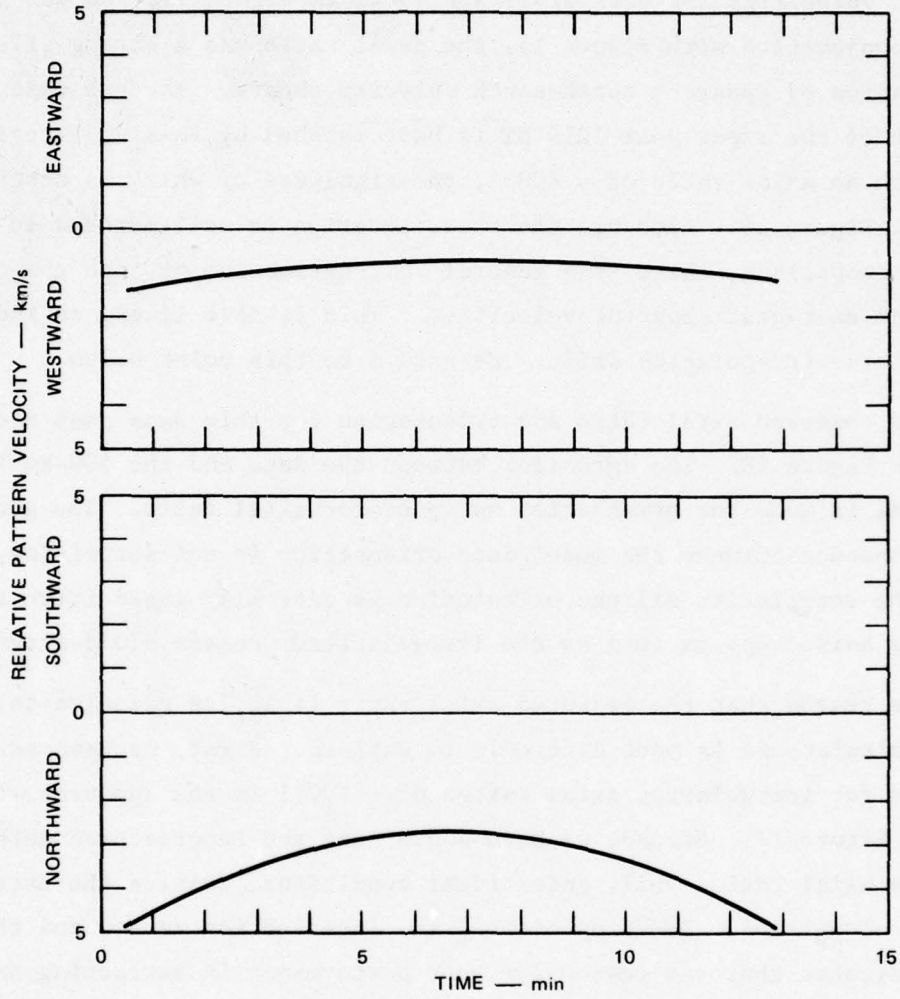

FIGURE 16 RELATIVE IRREGULARITY DRIFTS FOR THE EQUATORIAL WIDEBAND PASS SHOWN IN FIGURE 14, SATELLITE-INDUCED COMPONENT ONLY

All in all, this indicates that under ideal conditions we should obtain axial ratio, orientation, and relative drifts accurate to a few percent for 100:1 in situ, rod-like, F-region irregularities for more than half of a typical satellite pass. For the remainder of the pass good anisotropy but poor relative drift estimates are expected.

We next consider the experimental data for a high-elevation Kwajalein data set, pass 27-19. The geometry of this pass was used to generate the model calculations of Figures 14 through 16. The north-south and east-west

apparent velocities for pass 27-19 are shown in Figure 17. As was pointed out in conjunction with Figure 15, the axial ratio has a strong effect on the location of apparent north-south velocity shears. In this case, the location of the shear near 1219 UT is best matched by in-situ F-region rods with an axial ratio of $\sim$ 100:1, the signature of which is superimposed in Figure 15. Although the shear location is well-matched in time in this comparison, there is a general underestimation of both the north-south and east-west apparent velocities. This is most likely an indication of true irregularity drift. We return to this point below.

The observed axial ratio and orientation for this same pass are shown in Figure 18. The agreement between the data and the 500-km 100:1 rod model is good for orientation but poor for axial ratio. The good correspondence between the model/data orientation is not surprising, since the correlation ellipse orientation is generally insensitive to changing anisotropy as long as the irregularities remain field-aligned.

The reason that the measured axial ratio is so low relative to the model calculations is more difficult to explain. First, we have strong evidence for irregularity axial ratios of $\sim$ 100:1 in the apparent velocity data of Figure 17. Second, we have shown that the intersection method extracts axial ratios well, under ideal conditions, despite the extreme pattern elongation. Scrutiny of both the intersection method and the data indicates that one reason for poor performance in extracting axial ratio from real data could be that we do not have accurate enough estimates for the spaced-receiver antenna locations. This and other possibilities are being pursued further.

Although we currently have difficulty in obtaining anisotropy and relative drifts from the equatorial data, considerable information can be obtained from the apparent velocity data. For example, Figure 19 compares the measured apparent velocity data and the model calculations with 100 m/s, 200 m/s, and 300 m/s eastward F-region irregularity drifts. These drift magnitudes are consistent with other measures of the nighttime equatorial ionosphere (e.g., those of Woodman and La Hoz, 1976). Both the north-south and east-west measured apparent velocities are bracketed well by

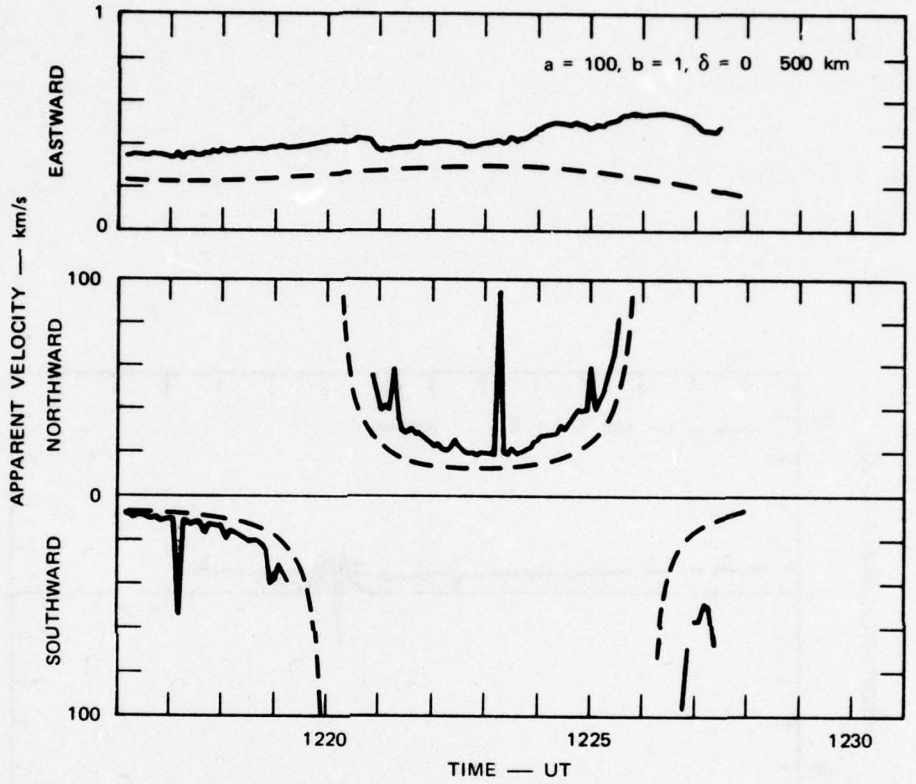

FIGURE 17 MEASURED AND CALCULATED APPARENT VELOCITIES, KWAJALEIN PASS 27-19, 26 AUGUST 1977

100:1 F-region rods, drifting between 100 and 300 m/s eastward. The primary shortcoming of this approach is that it is generally insensitive to any north-south drifts, which thus cannot be extracted. The general ambiguity between vertical and horizontal drifts [see Eqs. (4) and (5)] still remains.

As with the high-latitude data, a large number of equatorial passes suitable for spaced-receiver analysis have been collected. Detailed interpretation of this data and continued refinement of the method are under way. To date, information such as that in Figures 14 through 19 gives us preliminary but firm indications that axially symmetric, highly elongated, rod-like irregularities produce the bulk of the equatorial scintillation.

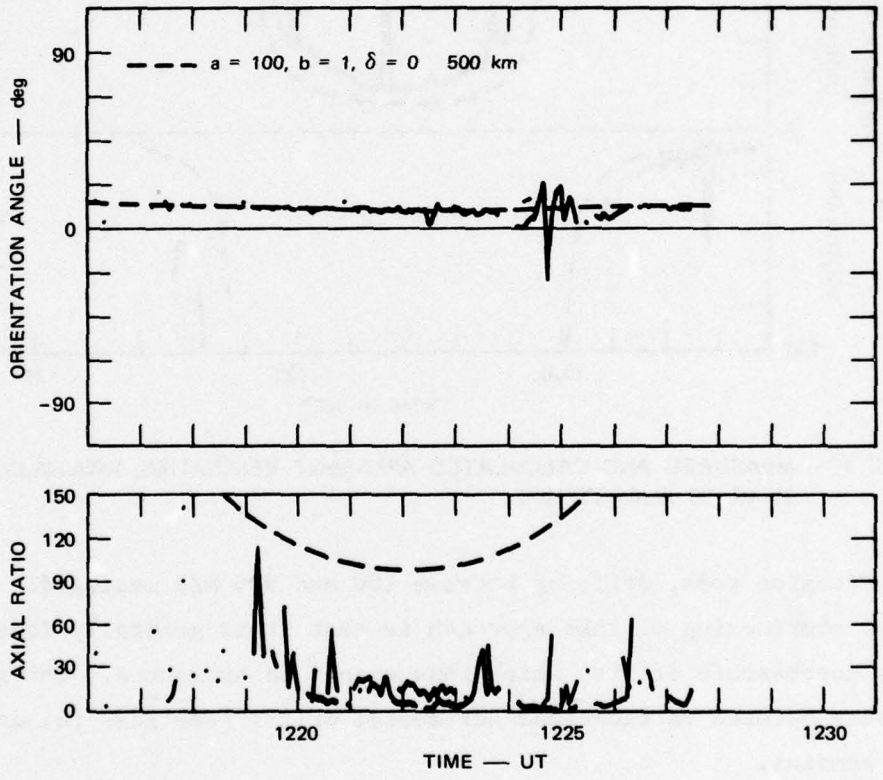

FIGURE 18 MEASURED AND CALCULATED AXIAL RATIO AND ORIENTATION ANGLE, KWAJALEIN PASS 27-19, 26 AUGUST 1977

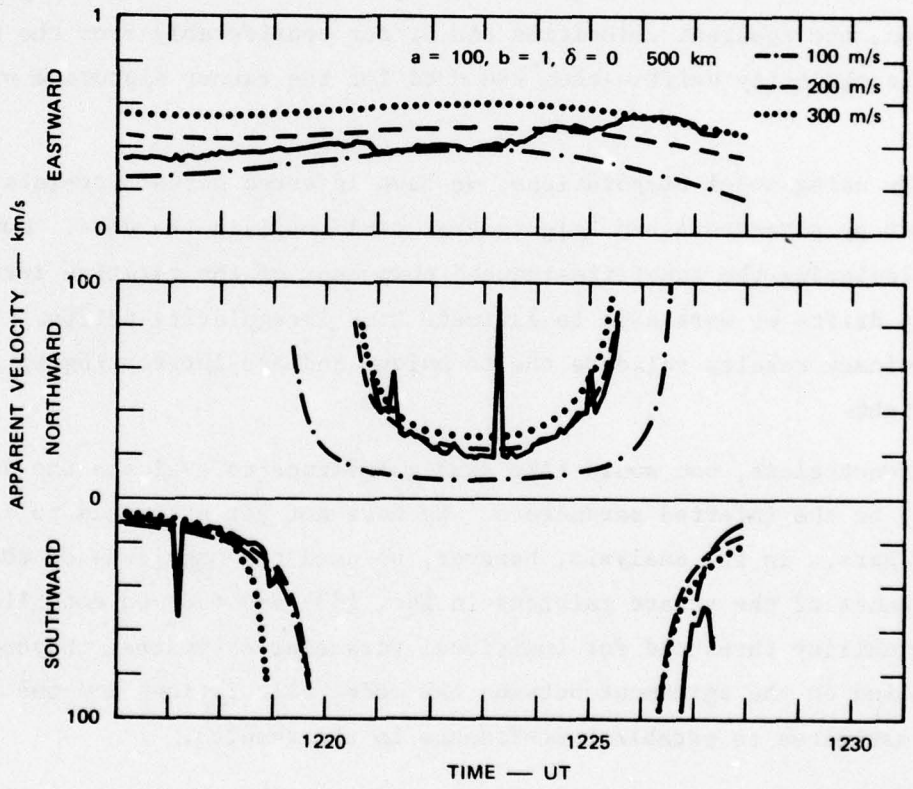

FIGURE 19 MEASURED AND CALCULATED APPARENT VELOCITIES WITH EASTWARD IRREGULARITY DRIFTS INCLUDED, KWAJALEIN PASS 27-19, 26 AUGUST 1977

V DISCUSSION

We have developed and demonstrated a technique (actually suggested by Armstrong and Coles, 1972) for simultaneously estimating the anisotropy and relative irregularity drifts of a radio wave diffraction pattern. Because of the complicated geometric dependence of the scattering phenomenon, the apparent velocities can differ considerably from the relative irregularity drifts--thus the need for the rather elaborate procedure.

By using model computations, we have inferred actual irregularity anisotropy parameters and heights that could explain the data. Moreover, by calculating the satellite-induced component of the relative irregularity drifts we were able to estimate true irregularity drifts. The preliminary results validate the technique and are interesting in their own right.

Nonetheless, one would like some guidelines to evaluate the uncertainty in the inferred parameters. We have not yet attempted to derive error bars. In the analysis, however, we used the magnitude of the determinants of the square matrices in Eqs. (33) and (38) to establish an acceptability threshold for individual parameter estimates. Beyond this, we relied on the agreement between the model calculations and the parameter estimates to establish confidence in the results.

There are also practical considerations. The sample interval and data block length critically influence the precision that can be obtained. The Wideband Satellite spaced-receiver system uses four fully coherent spaced receivers. Thus, the anisotropy and drift parameters can be independently determined from the phase and amplitude correlation functions. Since phase decorrelates much more slowly than amplitude, the latter is generally easier to use.

The amplitude and phase data are detrended as described in Fremouw et al. (1978) prior to the correlation function analysis. This procedure effectively establishes a common reference level for the signals, thereby minimizing normalization errors. The cross correlation delays τ_j and the intersections τ_{ij} are precisely determined by polynomial interpolation. By using an array processor, the data reduction for an entire $\sim$ 15-min pass is performed in less than 1 hour.

In summary, the apparent velocity parameter cannot be simply interpreted to obtain pattern drifts. Rather, an analysis procedure must be employed that simultaneously determines the anisotropy and relative drift of the diffraction pattern. We have described and demonstrated such a procedure in this report. In the next phase of analysis, procedures will be developed to automate the extraction of height and true drift estimates from the measured anisotropy and apparent pattern drifts.

REFERENCES

Armstrong, J. W. and W. A. Coles, "Analysis of Three-Station Interplanetary Scintillation," J. Geophys. Res., 77, 25, p. 4602, 1972.

Briggs, B. H., G. J. Phillips, and D. H. Shinn, "The Analysis of Observations on Spaced Receivers of the Fading of Radio Signals," Proc. Phys. Soc., B63, p. 106, 1950.

Fedor, L. S., "A Statistical Approach to the Determination of Three-Dimensional Ionospheric Drifts," J. Geophys. Res., 72, 21, p. 5401, 1967.

Fremouw, E. J., R. L. Leadabrand, R. C. Livingston, M. D. Cousins, C. L. Rino, B. C. Fair, and R. A. Long, "Early Results from the DNA Wideband Satellite Experiment--Complex-Signal Scintillation," Radio Sci., 13, 1, p. 167, 1978.

Mitra, A. N., "A Radio Method of Measuring Winds in the Ionosphere," Proc. IRE, 96, p. 441, 1949.

Moorcroft, D. R. and K. A. Arima, "The Shape of the F-Region Irregularities which Produce Satellite Scintillations--Evidence for Axial Asymmetry," J. Atmos. Terr. Phys., 34, p. 437, 1972.

Phillips, G. J. and M. Spencer, "The Effects of Anisometric Amplitude Patterns in the Measurement of Ionospheric Drifts," Proc. Roy. Soc., B68, p. 481, 1955.

Rino, C. L., "Iterative Methods for Treating the Multiple Scattering of Radio Waves," accepted for publication, J. Atmos. Terr. Phys., 1978.

Rino, C. L. and E. J. Fremouw, "The Angle Dependence of Singly Scattered Wavefields," J. Atmos. Terr. Phys., 39, p. 859, 1977.

Rino, C. L. and S. J. Matthews, "On the Interpretation of Ionospheric Scintillation Data Using a Power-Law Phase Screen Model--Weak Scatter," Topical Report 2, DNA 4606T, Contract DNA001-77-C-0220, SRI Project 6434, SRI International, Menlo Park, CA, 1978.

Singleton, D. G., "Dependence of Satellite Scintillations on Zenith Angle and Azimuth," J. Atmos. Terr. Phys., 32, p. 789, 1970.

Woodman, R. F. and C. La Hoz, "Radar Observations of F. Region Equatorial Irregularities," J. Geophys. Res., 81, p. 5447, 1976.

Wright, J. W. and M. L. V. Pitteway, "Computer Simulation of Ionospheric Radio Drift Measurements, and Their Analysis by Correlation Methods," Radio Sci., 13, p. 189, 1978.

Yerg, D. G., "Notes on Correlation Methods for Evaluating Ionospheric Winds from Radio Fading Records," J. Geophys. Res., 60, p. 173, 1955.

Appendix A

ANISOTROPY COEFFICIENTS

In Rino and Fremouw (1977) it is shown that the two-dimensional phase SDF, $\Phi_{\delta\phi}(\vec{\kappa})$, is related to the three-dimensional irregularity SDF $\Phi_{\Delta N_e}(\vec{\kappa},\kappa_z)$ by the relation

$$\Phi_{\delta\phi}(\vec{\kappa}) = r_e^2\lambda^2 L \sec^2\theta\, \Phi_{\Delta N_e}(\vec{\kappa}, -\tan\theta\, \hat{a}_{k_T}\, \vec{\kappa}) \quad . \tag{A-1}$$

Now, if we assume that there exists a coordinate system (r, s, t) in which the three-dimensional spatial correlation depends only on $[\Delta r^2 + (\Delta s/a)^2 + (\Delta t/r)^2]^{1/2}$, with a and b $\geq$ 1, the corresponding functional dependence of $\Phi_{\Delta N_e}(\vec{\kappa}, \kappa_z)$ on $\vec{\kappa}$ and κ_z can be computed by straightforward manipulations.

For the coordinate system of Figure 1, the functional dependence is given in terms of the quadratic form $[(\vec{\kappa}, \kappa_z)^T \underset{\sim}{\hat{C}}(\vec{\kappa}, \kappa_z)]^{1/2}$ where $\underset{\sim}{\hat{C}}$ is a 3 × 3 matrix with elements:

$$\hat{C}_{11} = a^2 \cos^2\psi + \sin^2\psi(b^2 \sin^2\delta + \cos^2\delta) \tag{A-2a}$$

$$\hat{C}_{22} = b^2 \cos^2\delta + \sin^2\delta \tag{A-2b}$$

$$\hat{C}_{33} = a^2 \sin^2\psi + \cos^2\psi(b^2 \sin^2\delta + \cos^2\delta) \tag{A-2c}$$

$$\hat{C}_{12} = \hat{C}_{21} = (b^2 - 1) \sin\psi \sin\delta \cos\delta \tag{A-2d}$$

$$\hat{C}_{13} = \hat{C}_{31} = (a^2 - b^2 \sin^2\delta - \cos^2\delta) \sin\psi \cos\psi \tag{A-2e}$$

$$\hat{C}_{23} = \hat{C}_{32} = -(b^2 - 1) \cos\psi \sin\delta \cos\delta \quad . \tag{A-2f}$$

Appendix B

SOME USEFUL COORDINATE TRANSFORMATIONS

Earth-fixed spaced receivers are most conveniently measured in a system as shown in Figure 2 where z_R is positive upward and y_R is positive northward. The rotation to any other geographic system, say $x_p y_p z_p$, is given by the 3 × 3 matrix R with elements:

$$r_{11} = \cos \lambda_P \cos \lambda_R + \sin \lambda_P \sin \lambda_R \tag{B-1a}$$

$$r_{12} = (-\cos \lambda_P \sin \lambda_R + \sin \lambda_P \cos \lambda_R) \sin \varphi_R \tag{B-1b}$$

$$r_{13} = (\cos \lambda_P \sin \lambda_R - \sin \lambda_P \cos \lambda_R) \cos \varphi_R \tag{B-1c}$$

$$r_{21} = (-\sin \lambda_P \cos \lambda_R + \cos \lambda_P \sin \lambda_R) \sin \varphi_P \tag{B-1d}$$

$$r_{22} = (\sin \lambda_P \sin \lambda_R + \cos \lambda_P \cos \lambda_R) \sin \varphi_P \sin \varphi_R + \cos \varphi_P \cos \varphi_R \tag{B-1e}$$

$$r_{23} = -(\sin \lambda_P \sin \lambda_R + \cos \lambda_P \cos \lambda_R) \sin \varphi_P \cos \varphi_R + \cos \varphi_P \sin \varphi_R \tag{B-1f}$$

$$r_{31} = (\sin \lambda_P \cos \lambda_R - \sin \lambda_R \cos \lambda_P) \cos \varphi_P \tag{B-1g}$$

$$r_{32} = -(\sin \lambda_P \sin \lambda_R + \cos \lambda_P \cos \lambda_R) \cos \varphi_P \sin \varphi_R + \sin \varphi_P \cos \varphi_R \tag{B-1h}$$

$$r_{33} = (\sin \lambda_P \sin \lambda_R + \cos \lambda_P \cos \lambda_R) \cos \varphi_P \cos \varphi_R + \sin \varphi_P \sin \varphi_R \tag{B-1i}$$

where λ_R and λ_P denote the respective longitudes and φ_R denotes the respective latitudes.

To transform a point from the $x_R y_R z_R$ system to the xyz system, a second rotation and a reflection are required; this is implemented by multiplying by the matrix $\underset{\sim}{D}$. If δ represents the magnetic declination angle, then

The angle ψ is shown in Figure 1. The angle δ is the orientation angle of the transverse irregularity axis. Thus, if we take s to lie along the local magnetic field direction, ψ is the dip angle.

The coefficients A, B, and C are readily deduced by substituting $-\tan\theta\ \hat{a}_{k_T} \cdot \vec{\kappa}$ for κ_z and collecting the terms multiplying κ_x^2, $\kappa_x\kappa_y$, and κ_y^2. The result of these manipulations gives the desired expressions:

$$A = [\hat{C}_{11} + \hat{C}_{33} \tan^2\theta \cos^2\varphi - 2\hat{C}_{13} \tan\theta \cos\varphi] \qquad \text{(A-3a)}$$

$$B = 2[\hat{C}_{12} + \hat{C}_{33} \tan^2\theta \sin\varphi \cos\varphi - \tan\theta\ (\hat{C}_{13} \sin\varphi + \hat{C}_{23} \cos\varphi)] \qquad \text{(A-3b)}$$

$$C = [\hat{C}_{22} + \hat{C}_{33} \tan^2\theta \sin^2\varphi - 2\hat{C}_{23} \tan\theta \sin\varphi] \quad . \qquad \text{(A-3c)}$$

We note that if a = b = 1 (isotropic irregularities), then

$$A = 1 + \tan^2\theta \cos^2\varphi \qquad \text{(A-4a)}$$

$$B = 2 \tan^2\theta \sin\varphi \cos\varphi \qquad \text{(A-4b)}$$

$$C = 1 + \tan^2\theta \sin^2\varphi \quad . \qquad \text{(A-4c)}$$

Thus, the diffraction pattern is not, in general, isotropic, even if the irregularities themselves are isotropic.

Appendix B

SOME USEFUL COORDINATE TRANSFORMATIONS

Earth-fixed spaced receivers are most conveniently measured in a system as shown in Figure 2 where z_R is positive upward and y_R is positive northward. The rotation to any other geographic system, say $x_p y_p z_p$, is given by the 3 × 3 matrix R with elements:

$$r_{11} = \cos \lambda_P \cos \lambda_R + \sin \lambda_P \sin \lambda_R \tag{B-1a}$$

$$r_{12} = (-\cos \lambda_P \sin \lambda_R + \sin \lambda_P \cos \lambda_R) \sin \varphi_R \tag{B-1b}$$

$$r_{13} = (\cos \lambda_P \sin \lambda_R - \sin \lambda_P \cos \lambda_R) \cos \varphi_R \tag{B-1c}$$

$$r_{21} = (-\sin \lambda_P \cos \lambda_R + \cos \lambda_P \sin \lambda_R) \sin \varphi_P \tag{B-1d}$$

$$r_{22} = (\sin \lambda_P \sin \lambda_R + \cos \lambda_P \cos \lambda_R) \sin \varphi_P \sin \varphi_R + \cos \varphi_P \cos \varphi_R \tag{B-1e}$$

$$r_{23} = -(\sin \lambda_P \sin \lambda_R + \cos \lambda_P \cos \lambda_R) \sin \varphi_P \cos \varphi_R + \cos \varphi_P \sin \varphi_R \tag{B-1f}$$

$$r_{31} = (\sin \lambda_P \cos \lambda_R - \sin \lambda_R \cos \lambda_P) \cos \varphi_P \tag{B-1g}$$

$$r_{32} = -(\sin \lambda_P \sin \lambda_R + \cos \lambda_P \cos \lambda_R) \cos \varphi_P \sin \varphi_R + \sin \varphi_P \cos \varphi_R \tag{B-1h}$$

$$r_{33} = (\sin \lambda_P \sin \lambda_R + \cos \lambda_P \cos \lambda_R) \cos \varphi_P \cos \varphi_R + \sin \varphi_P \sin \varphi_R \tag{B-1i}$$

where λ_R and λ_P denote the respective longitudes and φ_R denotes the respective latitudes.

To transform a point from the $x_R y_R z_R$ system to the xyz system, a second rotation and a reflection are required; this is implemented by multiplying by the matrix $\underset{\sim}{D}$. If δ represents the magnetic declination angle, then

$$\underset{\sim}{D} = \begin{pmatrix} \sin\delta & \cos\delta & 0 \\ \cos\delta & -\sin\delta & 0 \\ 0 & 0 & 1 \end{pmatrix} \quad . \tag{B-2}$$

The overall transformation is denoted by the 3 × 3 matrix $\underset{\sim}{S} = \underset{\sim\sim}{DR}$ with elements s_{ij}.

Now, as shown in Section III, contours of constant correlations of intensity or phase are defined by constant values of

$$f^2(\vec{\Delta}\rho_s) = \Delta\vec{\rho}_s{}^T \underset{\sim}{\mathcal{E}} \Delta\vec{\rho}_s \quad . \tag{B-3}$$

If $\vec{\Delta}R$ represents a vector in the $x_R y_R z_R$ system, the 2-vector $\Delta\vec{\rho}_s$ is obtained by first generating $\underset{\sim}{S}\,\vec{\Delta}R$ and then using the definition of $\Delta\vec{\rho}_s$ in Eq. (4). The overall manipulation can be represented by the 2 × 3 matrix S′ with elements:

$$s'_{11} = s_{11} + \tan\theta \cos\varphi\, r_{31} \tag{B-4a}$$

$$s'_{12} = s_{12} + \tan\theta \cos\varphi\, r_{32} \tag{B-4b}$$

$$s'_{13} = s_{13} + \tan\theta \cos\varphi\, r_{33} \tag{B-4c}$$

$$s'_{21} = s_{21} + \tan\theta \cos\varphi\, r_{31} \tag{B-4d}$$

$$s'_{22} = s_{22} + \tan\theta \sin\varphi\, r_{32} \tag{B-4e}$$

$$s'_{23} = s_{23} + \tan\theta \sin\varphi\, r_{33} \quad . \tag{B-4f}$$

In terms of $\underset{\sim}{S}'$, therefore,

$$f^2(\Delta\vec{\rho}_s) = \vec{\Delta}R^T \underset{\sim}{S}'^T \underset{\sim}{\mathcal{E}} \underset{\sim}{S}\, \Delta R \quad . \tag{B-5}$$

DISTRIBUTION LIST

DEPARTMENT OF DEFENSE

Assistant Secretary of Defense
Comm. Cmd. Cont. & Intell.
ATTN: Dir. of Intelligence Systems, J. Babcock
ATTN: C3IST&CCS, M. Epstein

Assistant to the Secretary of Defense
Atomic Energy
ATTN: Executive Assistant

Command & Control Technical Center
Department of Defense
ATTN: C-650, G. Jones
ATTN: C-312, R. Mason
3 cy ATTN: C-650, W. Heidig

Defense Advanced Rsch. Proj. Agency
ATTN: TIO

Defense Communications Agency
ATTN: Code 101B
ATTN: Code 480
ATTN: Code 810, J. Barna
ATTN: Code 205
ATTN: Code R1033, M. Raffensperger

Defense Communications Engineer Center
ATTN: Code R720, J. Worthington
ATTN: Code R410, J. McLean
ATTN: Code R123

Defense Documentation Center
12 cy ATTN: DD

Defense Intelligence Agency
ATTN: DB-4C, E. O'Farrell
ATTN: DC-7D, W. Wittig
ATTN: DT-1B
ATTN: DB, A. Wise
ATTN: DT-5
ATTN: HQ-TR, J. Stewart

Defense Nuclear Agency
ATTN: STVL
ATTN: DDST
4 cy ATTN: TITL
3 cy ATTN: RAAE

Field Command
Defense Nuclear Agency
ATTN: FCPR

Field Command
Defense Nuclear Agency
Livermore Division
ATTN: FCPRL

Interservice Nuclear Weapons School
ATTN: TTV

Joint Chiefs of Staff
ATTN: J-3, WWMCCS Evaluation Office
2 cy ATTN: J-37/C3S

Undersecretary of Def. for Rsch. & Engrg.
ATTN: Strategic & Space Systems (OS)

DEPARTMENT OF DEFENSE (Continued)

Joint Strat. Tgt. Planning Staff
ATTN: JLTW-2
ATTN: JPST, G. Goetz

National Security Agency
ATTN: R-52, J. Skillman
ATTN: W-32, O. Bartlett
ATTN: B-3, F. Leonard

WWMCCS System Engineering Org.
ATTN: R. Crawford

DEPARTMENT OF THE ARMY

Assistant Chief of Staff for Automation & Comm.
Department of the Army
ATTN: DAAC-ZT, P. Kenny

Atmospheric Sciences Laboratory
U.S. Army Electronics R & D Command
ATTN: DELAS-EO, F. Niles

BMD Systems Command
Department of the Army
2 cy ATTN: BMDSC-HW

Deputy Chief of Staff for Ops. & Plans
Department of the Army
ATTN: DAMO-RQC

Electronics Tech. & Devices Lab.
U.S. Army Electronics R & D Command
ATTN: DELET-ER, H. Bomke

Harry Diamond Laboratories
Department of the Army
ATTN: DELHD-N-P, F. Wimenitz
ATTN: DELHD-I-TL, M. Weiner
ATTN: DELHD-N-RB, R. Williams
ATTN: DELHD-N-P

U.S. Army Comm-Elec. Engrg. Instal. Agency
ATTN: CCC-CED-CCO, W. Neuendorf
ATTN: CCC-EMEO-PED, G. Lane
ATTN: CCC-EMEO, W. Nair

U.S. Army Communications Command
ATTN: CC-OPS-WR, H. Wilson
ATTN: CC-OPS-W

U.S. Army Communications R&D Command
ATTN: DRDCO-COM-RY, W. Kesselman

U.S. Army Foreign Science & Tech. Ctr.
ATTN: DRXST-SD

U.S. Army Materiel Dev. & Readiness Cmd.
ATTN: DRCLDC, J. Bender

U.S. Army Nuclear & Chemical Agency
ATTN: Library

U.S. Army Satellite Comm. Agency
ATTN: Document Control

DEPARTMENT OF THE ARMY (Continued)

U.S. Army TRADOC Systems Analysis Activity
ATTN: ATAA-TDC
ATTN: ATAA-TCC, F. Payan, Jr.
ATTN: ATAA-PL

DEPARTMENT OF THE NAVY

Joint Cruise Missile Project Office
Department of the Navy
ATTN: JCM-G-70

Naval Air Development Center
ATTN: Code 6091, M. Setz

Naval Air Systems Command
ATTN: PMA 271

Naval Electronic Systems Command
ATTN: Code 501A
ATTN: Code 3101, T. Hughes
ATTN: PME 117-20
ATTN: PME 106-4, S. Kearney
ATTN: PME 117-211, B. Kruger
ATTN: PME 106-13, T. Griffin
ATTN: PME 117-2013, G. Burnhart

Naval Intelligence Support Ctr.
ATTN: NISC-50

Naval Ocean Systems Center
ATTN: Code 5322, M. Paulson
ATTN: Code 532, J. Bickel
ATTN: Code 8151, C. Baggett
3 cy ATTN: Code 5324, W. Moler

Naval Research Laboratory
ATTN: Code 6701, J. Brown
ATTN: Code 7555
ATTN: Code 6700, T. Coffey
ATTN: Code 6707, J. Davis
ATTN: Code 7500, B. Wald
ATTN: Code 7580

Naval Space Surveillance System
ATTN: J. Burton

Naval Surface Weapons Center
ATTN: Code F31

Naval Surface Weapons Center
ATTN: Code F-14, R. Butler

Naval Telecommunications Command
ATTN: Code 341

Office of Naval Research
ATTN: Code 421
ATTN: Code 420

Office of the Chief of Naval Operations
ATTN: OP 604C
ATTN: OP 941D
ATTN: OP 981N

Strategic Systems Project Office
Department of the Navy
ATTN: NSP-2141
ATTN: NSP-43
ATTN: NSP-2722, F. Wimberly

DEPARTMENT OF THE AIR FORCE

Aerospace Defense Command
Department of the Air Force
ATTN: DC, T. Long

Aerospace Defense Command
Department of the Air Force
ATTN: XPDQ
ATTN: XP

Air Force Avionics Laboratory
ATTN: AAD, W. Hunt
ATTN: AAD, A. Johnson

Air Force Geophysics Laboratory
ATTN: OPR-1, J. Ulwick
ATTN: PHI, J. Buchau
ATTN: LKB, K. Champion
ATTN: OPR, A. Stair
ATTN: PHP, J. Aarons
ATTN: PHP, J. Mullen

Air Force Weapons Laboratory, AFSC
ATTN: DYC
ATTN: SUL

Air Logistics Command
Department of the Air Force
ATTN: OO-ALC/MM, R. Blackburn

Assistant Chief of Staff
Intelligence
Department of the Air Force
ATTN: INED

Assistant Chief of Staff
Studies & Analysis
Department of the Air Force
ATTN: AF/SASC, G. Zank
ATTN: AF/SASC, W. Adams

Deputy Chief of Staff
Operations Plans and Readiness
Department of the Air Force
ATTN: AFXOKCD
ATTN: AFXOXFD
ATTN: AFXOKS
ATTN: AFXOKT

Deputy Chief of Staff
Research, Development, & Acq.
Department of the Air Force
ATTN: AFRDS
ATTN: AFRDSP
ATTN: AFRDSS
ATTN: AFRDQ

Electronic Systems Division
ATTN: DCKC, J. Clark

Electronic Systems Division
ATTN: YSM, J. Kobelski
ATTN: YSEA

Foreign Technology Division, AFSC
ATTN: NIIS Library
ATTN: SDEC, A. Oakes
ATTN: TQTD, B. Ballard

Electronic Systems Division
ATTN: XRW, J. Deas

DEPARTMENT OF THE AIR FORCE (Continued)

Rome Air Development Center, AFSC
ATTN: OCS, V. Coyne
ATTN: TSLD

Rome Air Development Center, AFSC
ATTN: EEP

Space & Missile Systems Organization
Air Force Systems Command
ATTN: MNNH
ATTN: MNNL, S. Kennedy

Space & Missile Systems Organization
Air Force Systems Command
ATTN: SKA, M. Clavin
ATTN: SKA, C. Rightmyer

Space & Missile Systems Organization
Air Force Systems Command
ATTN: SZJ, L. Doan

Strategic Air Command/XPFS
Department of the Air Force
ATTN: DCXT
ATTN: DCX
ATTN: DCXF
ATTN: OOKSN
ATTN: XPFS
ATTN: DCXT, T. Jorgensen
ATTN: NRT

OTHER GOVERNMENT AGENCIES

Central Intelligence Agency
ATTN: OSI/PSTD

Department of Commerce
National Bureau of Standards
ATTN: R. Moore

Department of Commerce
National Oceanic & Atmospheric Admin.
Environmental Research Laboratories
ATTN: Aeronomy Lab., G. Reid
ATTN: R. Grubb

Institute for Telecommunications Sciences
National Telecommunications & Info. Admin.
ATTN: A. Jean
ATTN: W. Utlaut
ATTN: L. Berry
ATTN: D. Crombie

U.S. Coast Guard
Department of Transportation
ATTN: G-DOE-3/TP54, B. Romine

DEPARTMENT OF ENERGY CONTRACTORS

Lawrence Livermore Laboratory
ATTN: Doc. Con. for Tech. Info. Dept., Library

Los Alamos Scientific Laboratory
ATTN: Doc. Con. for D. Westervelt
ATTN: Doc. Con. for P. Keaton
ATTN: Doc. Con. for R. Taschek

Sandia Laboratories
ATTN: Doc. Con. for T. Cook
ATTN: Doc. Con. for B. Murphey

DEPARTMENT OF ENERGY CONTRACTORS (Continued)

Sandia Laboratories
ATTN: Doc. Con. for Org. 1250, W. Brown
ATTN: Doc. Con. for D. Dahlgren
ATTN: Doc. Con. for 3141
ATTN: Doc. Con. for Space Project Div.
ATTN: Doc. Con. for D. Thornbrough

DEPARTMENT OF DEFENSE CONTRACTORS

Aerospace Corp.
ATTN: S. Bower
ATTN: D. Olsen
ATTN: N. Stockwell
ATTN: F. Morse
ATTN: V. Josephson
ATTN: I. Garfunkel
ATTN: R. Slaughter
ATTN: T. Salmi

University of Alaska
Geophysical Institute
ATTN: T. Davis
ATTN: N. Brown
ATTN: Technical Library

Analytical Systems Engineering Corp.
ATTN: Radio Sciences

Analytical Systems Engineering Corp.
ATTN: Security

Barry Research Communications
ATTN: J. McLaughlin

BDM Corp.
ATTN: T. Neighbors
ATTN: L. Jacobs

Berkeley Research Associates, Inc.
ATTN: J. Workman

Boeing Co.
ATTN: D. Murray
ATTN: G. Hall
ATTN: S. Tashird
ATTN: J. Kenney

University of California at San Diego
ATTN: H. Booker

Charles Stark Draper Lab., Inc.
ATTN: D. Cox
ATTN: J. Gilmore

Computer Sciences Corp.
ATTN: H. Blank

Comsat Labs
ATTN: G. Hyde
ATTN: R. Taur

Cornell University
Department of Electrical Engineering
ATTN: D. Farley, Jr.

EG&G, Inc.
ATTN: Doc Con. for J. Colvin
ATTN: Doc. Con. for D. Wright

DEPARTMENT OF DEFENSE CONTRACTORS (Continued)

Electrospace Systems, Inc.
ATTN: H. Logston

ESL, Inc.
ATTN: J. Marshall
ATTN: C. Prettie
ATTN: J. Roberts

Ford Aerospace & Communications Corp.
ATTN: J. Mattingley

General Electric Co.
Space Division
Valley Forge Space Center
ATTN: M. Bortner

General Electric Co.
Re-Entry & Environmental Systems Div.
ATTN: A. Steinmayer
ATTN: C. Zierdt
ATTN: S. Lipson

General Electric Co.
ATTN: F. Reibert

General Electric Co.-TEMPO
ATTN: T. Stevens
ATTN: M. Stanton
ATTN: DASIAC
ATTN: W. Knapp
ATTN: D. Chandler

General Electric Tech. Services Co., Inc.
ATTN: G. Millman

General Research Corp.
ATTN: J. Garbarino
ATTN: J. Ise, Jr.

GTE Sylvania, Inc.
Electronics Systems Grp-Eastern Div.
ATTN: M. Cross

HSS, Inc.
ATTN: D. Hansen

IBM Corp.
Federal Systems Division
ATTN: F. Ricci

University of Illinois
ATTN: K. Yeh

Institute for Defense Analyses
ATTN: J. Bengston
ATTN: E. Bauer
ATTN: J. Aein
ATTN: H. Wolfhard

International Tel. & Telegraph Corp.
ATTN: G. Wetmore
ATTN: Technical Library

Jaycor
ATTN: S. Goldman

Jaycor
ATTN: D. Carlos

DEPARTMENT OF DEFENSE CONTRACTORS (Continued)

Johns Hopkins University
Applied Physics Lab.
ATTN: Document Librarian
ATTN: T. Potemra
ATTN: B. Wise
ATTN: T. Evans
ATTN: J. Newland
ATTN: P. Komiske

Kaman Sciences Corp.
ATTN: T. Meagher

Linkabit Corp.
ATTN: I. Jacobs

Litton Systems, Inc.
Amecom Division
ATTN: R. Grasty

Lockheed Missiles & Space Co., Inc.
ATTN: D. Churchill
ATTN: Dept. 60-12

Lockheed Missiles and Space Co., Inc.
ATTN: R. Johnson
ATTN: W. Imhof
ATTN: M. Walt

M.I.T. Lincoln Lab.
ATTN: D. Towle
ATTN: L. Loughlin

McDonnell Douglas Corp.
ATTN: G. Mroz
ATTN: W. Olson
ATTN: N. Harris
ATTN: J. Moule

Mission Research Corp.
ATTN: R. Bogusch
ATTN: S. Gutsche
ATTN: D. Sowle
ATTN: R. Hendrick
ATTN: M. Scheibe
ATTN: F. Fajen

Mitre Corp.
ATTN: G. Harding
ATTN: C. Callahan
ATTN: A. Kymmel

Mitre Corp.
ATTN: M. Horrocks
ATTN: W. Foster
ATTN: W. Hall

Pacific-Sierra Research Corp.
ATTN: E. Field, Jr.

Pennsylvania State University
Ionosphere Research Lab.
ATTN: Ionospheric Research Lab.

Photometrics, Inc.
ATTN: I. Kofsky

Physical Dynamics, Inc.
ATTN: E. Fremouw

DEPARTMENT OF DEFENSE CONTRACTORS (Continued)

R & D Associates
ATTN: R. Lelevier
ATTN: M. Gantsweg
ATTN: H. Ory
ATTN: R. Turco
ATTN: C. Griefinger
ATTN: W. Wright, Jr.
ATTN: B. Gabbard
ATTN: W. Karzas
ATTN: C. MacDonald
ATTN: F. Gilmore

R & D Associates
ATTN: L. Delaney

Rand Corp.
ATTN: C. Crain
ATTN: E. Bedrozian

Riverside Research Institute
ATTN: V. Trapani

Rockwell International Corp.
Collins Telecommunications Sys. Division
ATTN: J. Kristof

Santa Fe Corp.
ATTN: E. Ortlieb

Utah State University
Space Measurements Lab.
ATTN: L. Jensen
ATTN: K. Baker

Visidyne, Inc.
ATTN: J. Carpenter

DEPARTMENT OF DEFENSE CONTRACTORS (Continued)

Science Applications, Inc.
ATTN: C. Smith
ATTN: D. Hamlin
ATTN: D. Sachs
ATTN: J. McDougall
ATTN: E. Straker
ATTN: L. Linson

Science Applications, Inc.
ATTN: D. Divis

Science Applications, Inc.
ATTN: SZ

SRI International
ATTN: A. Burns
ATTN: G. Price
ATTN: R. Leadabrand
ATTN: M. Baron
ATTN: G. Carpenter
ATTN: R. Livingston
ATTN: C. Rino
ATTN: W. Jaye
ATTN: W. Chesnut
ATTN: D. Neilson
ATTN: G. Smith

Teledyne Brown Engineering
ATTN: R. Deliberis

Tri-Com, Inc.
ATTN: D. Murray

TRW Defense & Space Sys. Group
ATTN: S. Altschuler
ATTN: R. Plebuch
ATTN: D. Dee